MNRAS **000**, 1–24 (2015) Preprint 15 December 2016 Compiled using MNRAS LATEX style file v3.0

Intergalactic Lyman continuum photon budget in the past 5 billion years

Prakash Gaikwad[1⋆], Vikram Khaire[1,2], Tirthankar Roy Choudhury[1], and Raghunathan Srianand[2]
[1] *National Centre for Radio Astrophysics, Tata Institute of Fundamental Research, Pune 411007, India*
[2] *Inter-University Centre for Astronomy and Astrophysics (IUCAA), Post Bag 4, Pune 411007, India*

arXiv:1605.02738v2 [astro-ph.CO] 14 Dec 2016

ABSTRACT

We constrain the H I photoionization rate ($\Gamma_{\rm HI}$) at $z \lesssim 0.45$ by comparing the flux probability distribution function and power spectrum of the Lyα forest data along 82 QSO sightlines obtained using Cosmic Origins Spectrograph with models generated from smoothed particle hydrodynamic simulations. We have developed a module named "Code for Ionization and Temperature Evolution (CITE)" for calculating the intergalactic medium (IGM) temperature evolution from high to low redshifts by post-processing the GADGET-2 simulation outputs. Our method, that produces results consistent with other simulations, is computationally less expensive thus allowing us to explore a large parameter space. It also allows rigorous estimation of the error covariance matrix for various statistical quantities of interest. We find that the best-fit $\Gamma_{\rm HI}(z)$ increases with z and follows $(4 \pm 0.1) \times 10^{-14}\ (1+z)^{4.99\pm0.12}$ s^{-1}. At any given z the typical uncertainties $\Delta\Gamma_{\rm HI}/\Gamma_{\rm HI}$ are ~ 25 per cent which contains not only the statistical errors but also those arising from possible degeneracy with the thermal history of the IGM and cosmological parameters and uncertainties in fitting the QSO continuum. These values of $\Gamma_{\rm HI}$ favour the scenario where only QSOs contribute to the ionizing background at $z < 2$. Our derived 3σ upper limit on average escape fraction is 0.008, consistent with measurements of low-z galaxies.

Key words: cosmological parameters - cosmology: observations-intergalactic medium-QSOs: absorption lines-ultraviolet: galaxies

1 INTRODUCTION

It is believed that the H I gas in the intergalactic medium (IGM) got reionized at $z \geq 5.5$ (Madau et al. 1999; Becker et al. 2001; Fan et al. 2001, 2006; Robertson et al. 2010; Bolton et al. 2011; Planck Collaboration et al. 2015; Khaire et al. 2016). At subsequent epochs the IGM is maintained at a highly ionized state by ultra-violet background (UVB) radiation ($\lambda \leq 912$Å). This UVB is contributed by radiation from blackhole accretion in Quasi Stellar Objects (hereafter QSOs) and stellar light escaping from galaxies (see for example, Miralda-Escude & Ostriker 1990; Haardt & Madau 1996; Fardal et al. 1998; Shull et al. 1999). The stellar contribution to UVB depends crucially on the fraction of ionizing photons escaping the galaxies known as the escape fraction ($f_{\rm esc}$). The $f_{\rm esc}$, in principle, depends on various physical factors such as the galaxy mass, morphology, composition of the interstellar medium (ISM), spatial distribution of gas and supernova rates (Ricotti & Shull 2000; Gnedin et al. 2008; Fernandez & Shull 2011; Benson et al. 2013; Kim et al. 2013; Cen & Kimm 2015; Roy et al. 2015). As a result, there is no consensus among different models of $f_{\rm esc}$. Measuring $f_{\rm esc}$ directly from observations too is quite challenging. The reported values of $f_{\rm esc}$ at $2 \leq z \leq 4$ vary between 0.01 to 0.2 (Iwata et al. 2009; Boutsia et al. 2011; Nestor et al. 2013; Cooke et al. 2014; Siana et al. 2015; Mostardi et al. 2015; Micheva et al. 2015; Grazian et al. 2016; Smith et al. 2016; Vasei et al. 2016). At $z < 2$, apart from the detection of high $f_{\rm esc}$ in few individual galaxies (Deharveng et al. 2001; Bergvall et al. 2006; Leitet et al. 2013; Borthakur et al. 2014; Izotov et al. 2016; Leitherer et al. 2016), the 3σ upper limits on average $f_{\rm esc}$ obtained by stacking samples of galaxies is ≤ 0.02 (Cowie et al. 2009; Bridge et al. 2010; Siana et al. 2010; Rutkowski et al. 2016).

An alternate way of constraining $f_{\rm esc}$ (and hence the stellar contribution to the UVB) is by measuring H I photoionization rate ($\Gamma_{\rm HI}$) (see Inoue et al. 2006; Khaire et al. 2016). The $f_{\rm esc}$ also determines the shape of the UVB (Khaire & Srianand 2013) which is important for modeling the distribution of ions in the IGM detected in the QSO

⋆ E-mail: prakashg@ncra.tifr.res.in

© 2015 The Authors

spectra (Shull et al. 2014; Rahmati et al. 2016; Finn et al. 2016; Oppenheimer et al. 2016). The UVB estimated at any given redshift z_0 depends on emissivities of radiating sources and the IGM opacity (contributed mainly by the Lyman Limit Systems with $N_{\rm HI} \geq 10^{17}$ cm^{-2}) over the large redshift range $z \geq z_0$. Therefore, measurements of $\Gamma_{\rm HI}(z_0)$, can be useful to constrain the IGM opacity evolution at $z \geq z_0$, especially at low-z where it is ill-constrained.

$\Gamma_{\rm HI}$ is usually constrained in the literature using three methods: (i) The first method uses the H I absorption in the proximity of QSOs (Bajtlik et al. 1988; Scott et al. 2000; Kulkarni & Fall 1993; Srianand & Khare 1996; Dall'Aglio et al. 2009; Calverley et al. 2011). The main uncertainties in this method arise because of the anisotropies in the QSO emission (Schirber et al. 2004; Kirkman & Tytler 2008) and possible density enhancements around the QSO host galaxies (Rollinde et al. 2005; Guimarães et al. 2007; Faucher-Giguère et al. 2008b). (ii) The second method, mainly useful at low-z, is based on the measured Hα surface brightness from the outskirts of nearby galaxies ($z \sim 0$) and high velocity cloud at the edges of our galaxy (Kutyrev & Reynolds 1989; Songaila et al. 1989; Vogel et al. 1995; Madsen et al. 2001; Weymann et al. 2001; Adams et al. 2011). However this measurement too is uncertain because of the assumptions made about the geometries of the Hα emitting gas (see Shull et al. 2014). (iii) The third method of constraining $\Gamma_{\rm HI}$ is by simulating the observed properties of the Ly-α forest (far away from the proximity of QSOs) such as the H I column density distribution function (CDDF) (Kollmeier et al. 2014; Shull et al. 2015), the flux probability distribution function (PDF) and the flux power spectrum (PS), which forms the basis of the analysis presented in this paper.

The basic idea behind using the Ly-α forest to constrain $\Gamma_{\rm HI}$ is that, under the fluctuating Gunn-Peterson approximation (hereafter FGPA; see Gunn & Peterson 1965; Weinberg et al. 1998; Croft et al. 1998), the Ly-α optical depth scales as $\Gamma_{\rm HI}^{-1}$ and hence can be used to constrain it. Observed statistical properties of the Ly-α forest are compared with those from an appropriate model with $\Gamma_{\rm HI}$ as one of the free parameters. The other free parameters in these models are those describing the thermal history of the IGM and the cosmological parameters which can be degenerate with $\Gamma_{\rm HI}$. To estimate the uncertainty in $\Gamma_{\rm HI}$ at $2 \leq z \leq 4$ due to its degeneracy with other parameters, Bolton et al. (2005); Bolton & Haehnelt (2007); Faucher-Giguère et al. (2008c) used scaling relations derived from their hydrodynamical simulations (Table 4 in Bolton & Haehnelt 2007). At these redshifts, it is well known from numerical simulations that the Ly-α forest arises from the low-density diffuse medium which accounts for 90 per cent of the baryons (Cen et al. 1994; Zhang et al. 1995; Hernquist et al. 1996; Miralda-Escudé et al. 1996; Rauch et al. 1997; Paschos & Norman 2005; Faucher-Giguère et al. 2008a; Bolton & Becker 2009). Hence a relatively simple model (Bi & Davidsen 1997; Choudhury et al. 2001) is sufficient to reliably constrain $\Gamma_{\rm HI}$. On the other hand at low-z ($z \leq 1.6$), only a small fraction ($\sim 30-40$ per cent) of the baryons are in diffuse medium responsible for Ly-α forest (Theuns et al. 1998a; Davé & Tripp 2001; Davé et al. 2010; Smith et al. 2011; Tepper-García et al. 2012; Shull et al. 2015). It turns out that a significant fraction ($\sim 30-50$ per cent) of the baryons are in a phase known as the warm hot intergalactic medium (WHIM) (Cen & Ostriker 1999; Davé et al. 2001; Cen & Ostriker 2006; Cen & Fang 2006; Lehner et al. 2007; Davé et al. 2010; Smith et al. 2011; Shull et al. 2012) and they are difficult to detect in either emission or absorption in the UV/optical bands. Hence to measure $\Gamma_{\rm HI}$ at low-z, one needs simulation incorporating all these effects. Furthermore there is also a strong possibility that SNe and AGN feedback processes can inject thermal energy into the IGM which may change the density-temperature distribution (i.e the phase diagram) of the baryons (Davé et al. 2010; Smith et al. 2011; Shull et al. 2015; Tepper-García et al. 2012), thus probably affecting the Ly-α forest observable.

To observe the low-z ($z \leq 1.6$) Ly-α forest, one needs the UV spectrograph onboard space based telescope. Thanks to a large survey using the Cosmic Origins Spectrograph (COS) onboard the Hubble Space Telescope (HST) (Danforth et al. 2016), there are now constraints on $\Gamma_{\rm HI}$, e.g., by using column density distribution of low-z Ly-α forest (Kollmeier et al. 2014; Shull et al. 2015), and by modeling the observed metal abundances of ions (Shull et al. 2014) using CLOUDY (Ferland et al. 1998). It turns out that there is a tension between the inferred $\Gamma_{\rm HI}$ by Kollmeier et al. (2014) and Shull et al. (2015), where both use Ly-α forest data by Danforth et al. (2016) but different simulations. The inferred $\Gamma_{\rm HI}$ values disagree by a factor of ~ 2.5. Given such a wide disagreement, it is worth taking an independent closer look at the $\Gamma_{\rm HI}$ measurements at low-z using the Ly-α forest, in particular a careful analysis of the systematics in the data as well as modeling uncertainties.

The main aim of this paper is to measure $\Gamma_{\rm HI}$ from the Ly-α forest data by Danforth et al. (2016), using two different statistics, namely the flux PDF and the flux PS that are regularly used in high-z studies. The method is based on performing smooth particle hydrodynamical (SPH) simulations to generate the density and velocity distributions of baryons and then post-processing the outputs to solve for the IGM temperature in presence of a UVB. For this purpose, we have developed a module, called the "Code for Ionization and Temperature Evolution" (CITE), to evolve the IGM temperature from high-z to the low-z of our interest. The advantage of this method is that it is computationally less expensive and sufficiently flexible to account for variations in the thermal history. Our analysis allows us to study the degeneracy between $\Gamma_{\rm HI}$ and parameters related to the thermal history. The other significant step in our analysis is that we calculate the errors on $\Gamma_{\rm HI}$, unlike Shull et al. (2015); Kollmeier et al. (2014), by estimating the error covariance matrix from the simulations using a method similar to Rollinde et al. (2013), thus avoiding any non-convergence that may arise from the limited sample of the observed data.

The plan of this paper is as follows: The observational data used in our analysis are discussed in §2. Details of the simulations, along with our method of calculating the temperature evolution, is discussed in §3. The two statistics used in this paper (i.e., the flux PDF and PS) and the associated errors are discussed in §4. The main results of our work are discussed in §5, where we match the simulations with the observed data to constrain $\Gamma_{\rm HI}$. We also discuss the various statistical and systematic uncertainties in the measured $\Gamma_{\rm HI}$, and show the consistency of our derived $\Gamma_{\rm HI}$ by comparing the H I column density distribution from observation with simulation. Fi-

nally we use the ionizing background computed by Khaire & Srianand (2015b) using the updated emissivities and IGM opacities to constrain $f_{\rm esc}$ from the evolution of $\Gamma_{\rm HI}$. We summarize our findings in §6. We use the flat ΛCDM cosmology with parameters $(\Omega_\Lambda, \Omega_m, \Omega_b, \sigma_8, n_s, h, Y) = (0.69, 0.31, 0.0486, 0.83, 0.96, 0.674, 0.24)$ (Planck Collaboration et al. 2015). All the distances are in comoving Mpc unless and otherwise mentioned. We use Γ_{12} to express $\Gamma_{\rm HI}$ in units of 10^{-12} s^{-1}.

2 HST-COS QSO ABSORPTION SPECTRA

We used the publicly available data from a survey[1] of low redshift Ly-α performed by Danforth et al. (2016) using HST-COS. The sample consists of 82 UV-bright QSO sightlines, with the QSOs being distributed across the redshift range 0.0628 to 0.852. The observations were carried out between July 2009 and August 2013. Using accurate data reduction process and careful subtraction of the background, Danforth et al. (2016) have produced high signal to noise ratio (SNR) Ly-α forest spectra in the observed wavelength range 1100Å to 1800Å. In addition, Danforth et al. (2016) have fitted the continuum and identified several thousand absorption features using a semi-automated procedure. These absorption features arise not only from H I Lyman series lines from the IGM but also from other intervening absorbers and from the Galactic interstellar medium. The redshift range for Ly-α lines covered by each sightline is shown in Fig.1. The sharp cutoff shown by blue curly bracket in the figure is because of the limited wavelength range covered by the spectrograph. We assume that a region of comoving size of up to $25h^{-1}$ cMpc around a QSO can be affected by the proximity effect of the QSO itself (Lidz et al. 2007), hence we exclude the corresponding section blueward of the Ly-α emission line.

We divide the data into 4 different redshift bins. Three bins are centered on $z = 0.2, 0.3, 0.4$ with a width of $\Delta z = 0.1$. We chose the lowest redshift bin $z = 0.1125$ with $\Delta z = 0.0375$ to avoid the contamination from the foreground geo-coronal line emission at $z < 0.075$. We are then left with Ly-α absorption from $50, 31, 16, 12$ sightlines each in the redshift bins with $z = 0.1125, 0.2, 0.3, 0.4$, respectively. The redshift bins chosen for analysis are indicated by roman numerals I, II, III and IV in Fig. 1. The values of the SNR for the Ly-α forest spectra vary between 5 and 17. Each observed spectrum has a resolution of ~ 17 km s^{-1}. Table 1 summarizes the properties of the observed Ly-α forest data in the four identified redshift bins. The table contains the redshift range of observation ($z_{\rm obs}$), the redshift of simulation box used ($\overline{z}_{\rm sim}$) for comparison, number of sightlines used and SNR range for each bin. A sample observed spectrum (towards the QSO 3C57) is shown in the top panel of Fig. 2. In addition to the Ly-α absorption, the spectrum contains higher Lyman-series and various metal absorption lines as shown in the figure. We fit these lines with gaussian and replace them with appropriate continuum added with gaussian random noise (with the same SNR) as shown in middle panel of Fig. 2. We use these clean spectra (i.e., metal line and higher order Ly-series line removed) to match observations with simulations using flux PDF and flux PS.

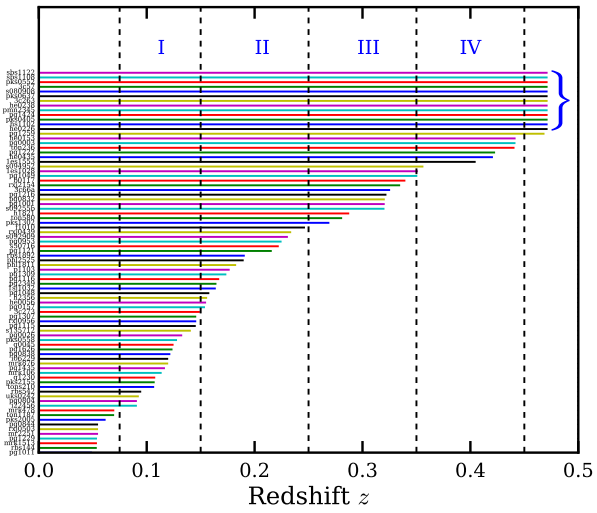

Figure 1. The redshift range covered by the Ly-α forest for the 82 HST-COS spectra used in this work (see §2). The vertical dashed lines show the redshift bins with centers at $z = 0.1125, 0.2, 0.3, 0.4$ and width $\Delta z = 0.075, 0.1, 0.1, 0.1$ respectively. The redshift bins used in this work are shown by roman numerals. The sharp cutoff shown by blue curly bracket is arising from the red wavelength cutoff of the COS-160M grism used (at $z = 0.48$). In these cases the COS spectra do not cover the Ly-α emission from the QSOs.

Table 1. Details of the HST-COS data used in different redshift bins. ($\overline{z}_{\rm sim}$ is redshift of simulation box used for comparison)

Redshift bin	$z_{\rm obs}$	$\overline{z}_{\rm sim}$	Number of QSOs	SNR Range
I	0.075 - 0.15	0.1	50	14.5 - 16.9
II	0.15 - 0.25	0.2	31	13.0 - 14.4
III	0.25 - 0.35	0.3	16	6.3 - 13.3
IV	0.35 - 0.45	0.4	12	5.8 - 6.9

3 DETAILS OF OUR SIMULATIONS

We generate the cosmological density and velocity fields using the smoothed particle hydrodynamic code GADGET-2[2] (Springel 2005). The initial conditions for the simulations are generated at a redshift $z = 99$ using the publicly available code 2LPT[3] (Scoccimarro et al. 2012). We use $1/30^{th}$ of the mean inter-particle distance as our gravitational softening length. The simulation outputs are stored at a redshift interval of 0.1 between $z = 2.1$ and $z = 0$. We use 2 simulation boxes containing 512^3 dark matter and an equal number of gas particles in a cubical box. Both simulation boxes are $50h^{-1}$ cMpc in size with different initial conditions. We use these boxes to study cosmic variance. As shown by Smith et al. (2011), the phase distribution of baryons in simulation box at low-z is converged if the box

[1] https://archive.stsci.edu/prepds/igm/

[2] http://www.mpa.mpa-garching.mpg.de/gadget/
[3] http://cosmo.nyu.edu/roman/2LPT/

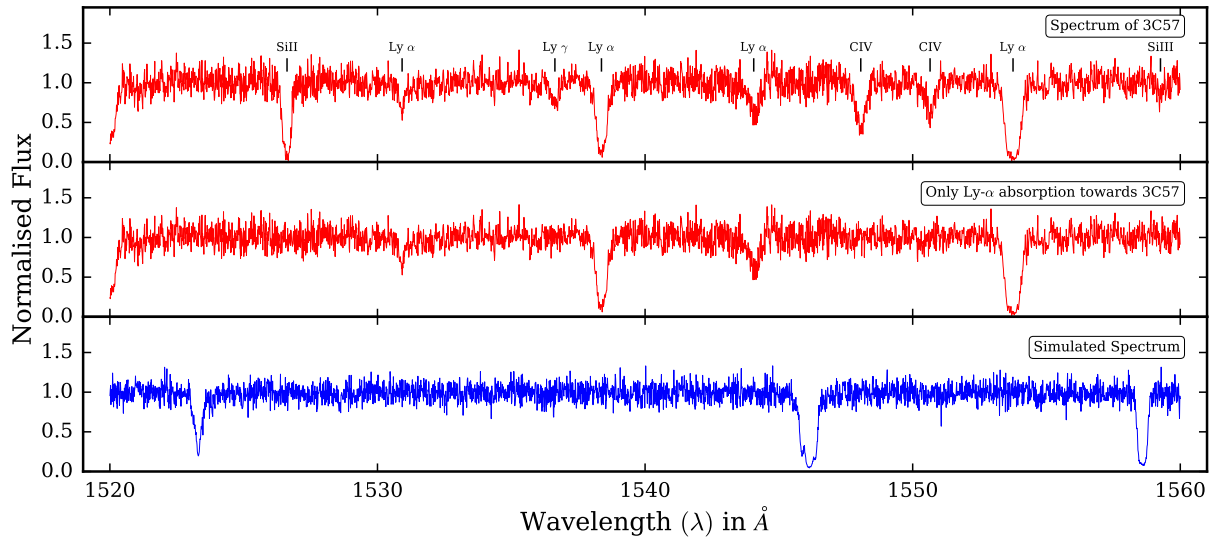

Figure 2. *Top panel* shows the observed Ly-α forest towards the QSO 3C57. H I Ly series and metal lines as identified by Danforth et al. (2016) are also marked. *Middle panel* shows the same spectrum after these lines are removed and replaced by a continuum added with random noise with the same SNR as in the original spectrum (see §2). *Bottom panel* shows the simulated spectrum towards a random line of sight in our simulation box. The simulated spectrum is convolved with the appropriate line spread function of HST-COS and added with noise having SNR similar to that of 3C57 (see §3.3).

size $50h^{-1}$ cMpc or above. The simulations used in this work do not include AGN feedback, outflows in the form of galactic wind or micro-turbulence. Note that the gas heating due to hydrodynamical processes arising from structure formation is incorporated in GADGET-2. However radiative heating and cooling processes are not incorporated in GADGET-2 and we include them in post processing step (see §3.2). We use GADGET-2 with post-processing instead of GADGET-3 in order to probe the wide range of parameter space. Later we compare our results with those obtained using different simulations in the literature.

3.1 Density, velocity and temperature

Each GADGET-2 output snapshot contains the position, velocity, internal energy per unit mass and smoothing length l of each smooth particle hydrodynamic (SPH) particle. We evaluate the above quantities on a uniform grid in the box using the smoothing kernel (Springel 2005),

$$W(r,l) = \frac{8}{\pi\, l^3} \begin{cases} 1 - 6\left(\frac{r}{l}\right)^2 + 6\left(\frac{r}{l}\right)^3, & 0 \le \frac{r}{l} \le \frac{1}{2} \\ 2\left(1 - \frac{r}{l}\right)^3, & \frac{1}{2} \le \frac{r}{l} \le 1 \\ 0, & \frac{r}{l} > 1 \end{cases} \quad (1)$$

where r is the distance between the grid point and the particle position. The density at the i^{th} grid is simply the sum of density contribution from all particle weighted by the smoothing kernel

$$\rho_i = \sum_{j=1}^{N} m_j\, W(|\mathbf{r}_{ij}|, l_j), \quad (2)$$

where N is the total number of particles, $|\mathbf{r}_{ij}|$ is the distance between the i^{th} grid point and j^{th} particle. m_j and l_j are the mass and smoothing length of the j^{th} particle respectively. The overdensity at the grid point i is given by

$$\Delta_i = \frac{\rho_i}{\overline{\rho}}, \quad \text{with} \quad \overline{\rho} = \frac{1}{N}\sum_{i=1}^{N} \rho_i \quad (3)$$

where $\overline{\rho}$ is the average density. In this work the symbol Δ is used for baryon overdensity. The density weighted estimate of any quantity f at the i^{th} grid point is given by

$$f_i = \frac{\sum_{j=1}^{N} f_j\, m_j\, W(|\mathbf{r}_{ij}|, l_j)}{\sum_{j=1}^{N} m_j\, W(|\mathbf{r}_{ij}|, l_j)} \quad (4)$$

where f_j is the value of the quantity for the j^{th} particle. The quantity f could be one of the velocity components (v_x, v_y, v_z) or the internal energy per unit mass u. The temperature of the gas as computed by GADGET-2, which we denote as T_g, can be obtained from the internal energy using the relation

$$T_g = \frac{2m_p}{3k_B}\, u, \quad (5)$$

here we have assumed a monoatomic gas composition with the ratio of specific heats given by 5/3. In the above expression, m_p is the mass of a proton and k_B is the Boltzmann's constant.

Fig. 3 shows a two-dimensional slice from our simulation box at $z = 0.3$. The left-hand panel and middle panel shows, respectively, the overdensity (Δ) and the temperature (T_g) of baryons as obtained from the GADGET-2 output snapshots. By comparing the left-hand and middle panels, one can see that the temperature distribution broadly traces the density distribution. This is related to the fact that the high density regions are heated because of hydrodynamical processes. Hereafter we will refer to this heating simply as shock heating. The temperature can be as high as $\sim 10^7$ K

in the vicinity of collapsed objects. The voids, on the other hand, remain extremely cool at temperatures ~ 10 K.

However, the above scenario does not capture all the relevant physics, in particular the photoheating of the low-density gas by UVB to higher temperatures and various cooling processes. It is indeed found from other simulations, that take into account the additional heating and cooling processes (Hui & Gnedin 1997; McDonald et al. 2001), that the temperature and density follow a reasonably tight relation (which we will refer to as the $T-\Delta$ relation) for mildly non-linear densities, i.e. $\Delta \leq 10$. As GADGET-2 does not include processes like the photoheating and radiative cooling, we find that the resulting temperature (T_g) and density relation does not show any power-law correlation.

This shortcoming has been addressed in subsequent versions of the GADGET, e.g., GADGET-3 (as discussed in Bolton et al. 2006) where one can perform the simulation in presence of a UVB. In this work, however, we follow a slightly different approach to account for the effects of photoionizing UVB and radiative cooling. Our method involves post-processing the GADGET-2 output to calculate the temperatures. We will show that this method produces results which are consistent with other works. The advantage of our method, however, is that we are able to explore the parameter space more efficiently without having to perform the full SPH simulation multiple times. In the following section we outline our method to evolve the IGM temperature in the post-processing step using 'Code for Ionization and Temperature Evolution' (CITE).

3.2 Code for Ionization and Temperature Evolution (CITE)

The temperature evolution equation for an overdense region in the IGM is given by (Hui & Gnedin 1997),

$$\begin{aligned}\frac{dT}{dt} &= \left(-2HT + \frac{2T}{3\Delta}\frac{d\Delta}{dt} + \frac{dT_{shock}}{dt}\right) \\ &+ \frac{T}{\sum_i X_i}\frac{d\sum_i X_i}{dt} + \frac{2}{3\,k_B\,n_b}\frac{dQ}{dt}. \end{aligned} \quad (6)$$

In the above equation the first three terms on right hand side (i.e., those in the large parenthesis) represent, respectively, the rate of cooling due to Hubble expansion, adiabatic heating and/or cooling arising from the evolution of the densities of gas particles and the change in temperature because of shocks which can be an important source of heating at low redshifts (Davé et al. 2001; Davé & Tripp 2001). These three mechanisms are taken into account in the default run of the GADGET-2. The fourth term on the right hand side represents the change in internal energy per particle arising from the change in the number of particles. The last term accounts for other heating and cooling processes, e.g., photo-heating and radiative cooling. The radiative cooling processes can, in principle, include cooling from recombinations, collisional ionization, collisional excitation, inverse Compton scattering and free-free emission.

As we discussed earlier, the default run of GADGET-2 results in temperatures that are too low at low densities, and does not show the tight $T-\Delta$ correlation at low to moderate overdensities. Therefore it is important to incorporate the effects of photoheating arising from the UVB to rectify the two problems. The method we follow to account for the photoheating and radiative cooling is as follows:

(i) We start with the output snapshots at a moderately high redshift, in our case it is taken to be $z_1 = 2.1$. This is an optimum redshift for our purpose as the He II reionization is likely to be completed by then (Kriss et al. 2001; Theuns et al. 2002; Zheng et al. 2004; Shull 2004; Khaire & Srianand 2013; Worseck et al. 2014) and thus the ionizing radiation can be taken to be uniform. If *all* the gas particles at z_1 follow a power-law equation of state, then the temperature would be given by[4]

$$\begin{aligned} T_1 \equiv T(z_1) &= T_0\,\Delta^{\gamma-1} \quad \text{for} \quad \Delta < 10 \\ &= T_0\,10^{\gamma-1} \quad \text{for} \quad \Delta \geq 10, \end{aligned} \quad (7)$$

where T_0 and γ are free parameters. We have assumed that the high density gas with $\Delta \geq 10$ is able to cool via atomic processes and hence have temperatures smaller than what is implied by the power-law (Theuns et al. 1998b). Note that the temperature obtained using Eq. 7, in general, will be different from that obtained from the GADGET-2 output which we denote as $T_{g,1} \equiv T_g(z_1)$.

To obtain the *actual* temperature of a gas particle, we use the following argument: If $T_{g,1} > T_1$ for that particle, then it may have been shock heated in a recent time step, and hence must have moved away from the $T-\Delta$ relation. In that case the particle temperature is taken to be $T_{g,1}$. Otherwise we assume the particle temperature to be following the equation of state and assign it as T_1.

We calculate the initial fractions of different ionized species (i.e., fraction of all ionization states of hydrogen and helium and hence the fraction of free electrons) by assuming ionization equilibrium to hold at the initial redshift $z_1 = 2.1$, which is a reasonable approximation for optically thin gas in the post-He II reionization era (Bolton et al. 2008; Becker et al. 2011). At this redshift we used $\Gamma_{\rm HI}$ consistent with QSO dominated ($f_{\rm esc} = 0$) Khaire & Srianand (2015a) (hereafter KS15) UVB.

(ii) Given the initial temperature and the ionization fractions, it is straightforward to calculate the last two terms on the right hand side of Eq. 6. The expressions for the heating and cooling rates used are taken from Theuns et al. (1998b) (for similar expressions see Sutherland & Dopita 1993; Katz et al. 1996; Weinberg et al. 1997; Wiersma et al. 2009). To estimate the photo-heating rate at any given z, we used QSO dominated (i.e. $f_{\rm esc} = 0$) KS15 UVB model.

(iii) To obtain the particle temperature at the next redshift $z_2 = z_1 - \Delta z$, we first compare the GADGET-2 temperatures $T_{g,1}$ and $T_{g,2}$ at the two redshifts and thereby check whether the gas particle is shock heated within that time interval. If for a particle $T_{g,2} < T_{g,1}$ then the particle is not shock heated. In this case we solve the Eq. 6 by neglecting third term (i.e., the one corresponding to the shock heating) on the right hand side. However if the particle is shock

[4] We varied the Δ cutoff in Eq. 7 from 10 to 5 and 15 and found that the resulting $T-\Delta$ relations at low-z are not sensitive to our choice of this cutoff.

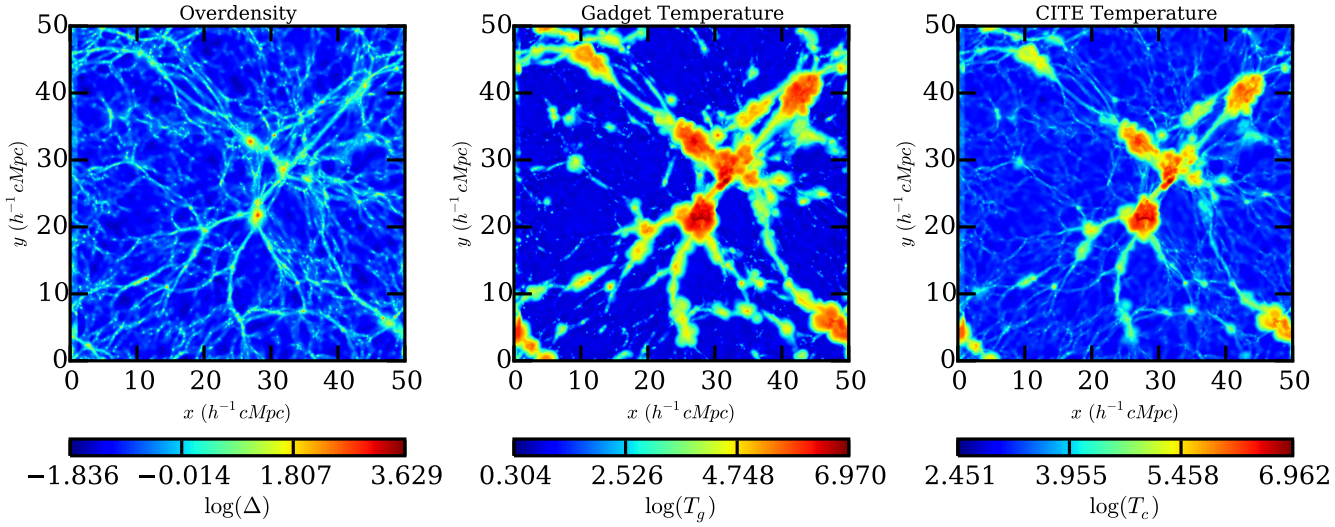

Figure 3. Two-dimensional slices of width 0.1 h^{-1} cMpc obtained from the GADGET-2 output snapshot at $z = 0.3$. *Left-hand panel:* the distribution of baryon overdensity Δ. Color scheme is such that red and blue color represent highest density and lowest density regions respectively. *Middle panel:* the gas temperature T_g from GADGET-2 (see §3.1). *Right-hand panel:* the gas temperature T predicted after evolving the temperature from $z_1 = 2.1$ (initially at z_1, $T_0 = 15000$ K and $\gamma = 1.3$) using our post-processing module CITE (see §3.2). The highly overdense regions are at higher temperatures because of the shock heating resulting from the structure formation. The color scheme in middle and right-hand panel is such that red and blue color corresponds to highest temperature and lowest temperature regions respectively.

heated[5] $T_{g,2} > T_{g,1}$ then we solve the same equation taking into account all the terms.

(iv) For redshift z_2 we solve *non-equilibrium* ionization evolution equation to calculate various ionization fractions. In addition to the photoionization, we also include the collisional ionization in the non-equilibrium ionization evolution equation.

(v) We then repeat the step (ii) to (iv) for subsequent redshifts and evolve the temperature of all the gas particles to our desired redshift.

Since the differential Eq. 6 is "stiff", it tends to be numerically unstable if the time-step between two snapshots is too large. To circumvent such difficulties, we divide the time-step between two neighboring redshifts into 100 smaller steps. We linearly interpolate the GADGET-2 temperature and densities for these intermediate time-steps. We have checked the effect of varying number of time-steps on $T-\Delta$ relation and found that the results converge as long as the number of intermediate steps is 50 or more. We incorporated the above method in a module called Code for Ionization and Temperature Evolution 'CITE'.

The *middle* and *right-hand* panels in Fig. 3 show the comparison between GADGET-2 temperature (T_g) and temperature from CITE (T_c). Note that the temperature scales in middle and right-hand panels are different. The highest temperature due to hydrodynamical processes is nearly same for T_g and T_c. But the lower temperature scale is considerably different due to additional processes incorporated through CITE. On an average, T_c also traces the density field shown in *left* hand panel of Fig. 3.

[5] We self consistently check if the particle is shock heated by solving Eq. 6 for GADGET-2 temperatures i.e., by using only the terms in the parenthesis on right hand side of Eq. 6.

Fig. 4 shows the resulting distribution at $z = 0.3$ in the $T-\Delta$ plane, which is often called as the "phase diagram". Note that the temperature and density plotted in the figure are volume-averaged, i.e., they are calculated by using the SPH kernel (see Eq. 4). For the plot we shoot 20000 random lines of sight through simulation box and calculate temperature and density on the grid points. The initial values at $z_1 = 2.1$ are chosen to be $T_0 = 15000$ K and $\gamma = 1.3$ (we refer to these values as initial T_0 and γ), the corresponding equation of state is shown by the red dashed line. The color coding represents density of points in logarithmic scale (i.e., the red color represents highest density of points). We can see from this figure that our simulation using CITE is able to produce the equation of state at low and moderate overdensities. In fact most of the grid points follow a power-law $T-\Delta$ relation (black dashed line) described by $T_0 = 4902$ K and $\gamma = 1.53$ (at $z = 0.3$) which is consistent with results from other low-z hydrodynamical simulations (Davé & Tripp 2001; Davé et al. 2010; Smith et al. 2011; Shull et al. 2012; Tepper-García et al. 2012; Shull et al. 2015). It is interesting to note that a significant fraction of points are at very high temperatures $T > 10^5$ K forming WHIM. We defer a detailed comparison of our simulations with those available in the literature to §3.4

3.3 Generating the Ly-α forest

The Ly-α forest is generated from the simulation box by shooting random lines of sight and storing the gas overdensities Δ, component of velocities and the CITE temperatures T on grid points along the line of sight . Assuming that there is no significant evolution in the gas properties within the redshift bin, we splice together the lines of sight in such a way that it covers a redshift path identical to the observed spectra. The spectra of the Ly-α transmitted flux (F) are

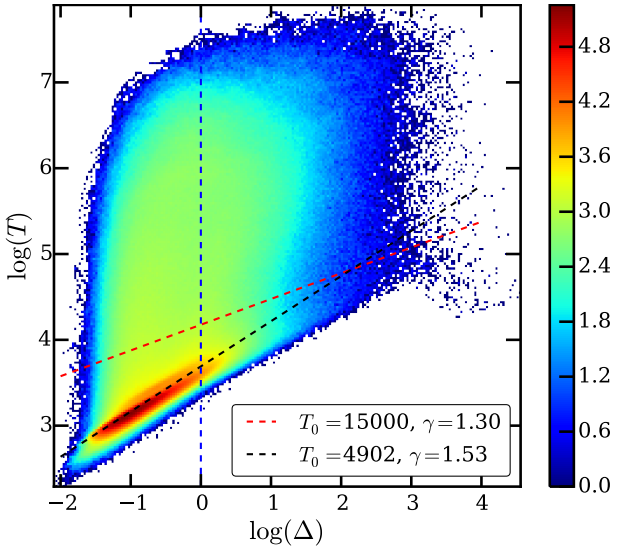

Figure 4. Distribution of grid points in the $T-\Delta$ plane at $z = 0.3$ when the temperatures are estimated using CITE (see §3.2 for details of CITE). The color scale indicates the density of points are shown (in logarithmic scale). At the initial redshift $z_1 = 2.1$ the values of the free parameters are chosen as $T_0 = 15000$ K and $\gamma = 1.3$ (model $T15 - \gamma 1.3$ in Table 3), to define the effective equation of state of the IGM shown by the red dashed line. The final equation of state at $z = 0.3$ is best described by parameters $T_0 = 4902$ K and $\gamma = 1.53$ (black dashed line).

generated using the procedure given in Choudhury et al. (2001) and Padmanabhan et al. (2015). There are essentially four steps in simulating the spectra: (i) The temperature, baryonic density field and peculiar velocity along the sightline is calculated using Eqs. 1 to 4 as explained in §3.1; (ii) The neutral hydrogen density ($n_{\rm HI}$) field along a sightline is obtained from the baryonic density field assuming photoionizing equilibrium with UVB; (iii) The $n_{\rm HI}$ field is then used for calculating the Ly-α optical depth τ at each pixel accounting for peculiar velocity effects and the thermal and natural widths of the line profile; (iv) The transmitted flux is given simply by $F = \exp(-\tau)$. Note that the spectra thus generated depend on initial conditions of the model (at $z_1 = 2.1$ refer Table 3) and the photoionization rate Γ_{12} ($\Gamma_{\rm HI}$ in units of 10^{-12} s^{-1}) at the redshift of interest ($z < 0.5$). To arrive at different self-consistent combinations of the two parameters T_0 and γ at the redshift of interest, we vary these two parameters at the initial redshift $z_1 = 2.1$ and calculate the temperature for each gas particle using CITE[6] mentioned in §3.2 and Table 3.

In order to enable fair comparison with the observational data, we prepare a sample of mock spectra which has properties resembling as close as possible to the observed ones. Each redshift bin contains different number of observed spectra (see Table 1). Let us assume that there are $N_{\rm spec}$ observed spectra at the redshift of interest z. For given thermal history and a free parameter $\Gamma_{\rm HI}$, we first generate $N_{\rm spec}$ simulated spectra using the method described above, which we call a "mock sample". We repeat the procedure by choosing different random sightlines and generate N such mock samples. We take $N = 500$ in this work. The collection of N mock samples constitute a "mock suite". Thus at z, the mock suite consists of $N \times N_{\rm spec}$ simulated spectra. The velocity separation of pixels in the simulated spectra is ~ 5 km s^{-1} which is set by the resolution of the box, whereas the velocity resolution of observations is ~ 17 km s^{-1}. We therefore resample the simulated spectra (by linear interpolation) to match the observed data and then convolve with the line spread function (LSF) given for HST-COS spectra. HST-COS LSF[7] is given at various wavelength line centers (λ_c) e.g. from 1150 Å to 1750Å in steps of 50Å. For our purpose we assume that the broadening function is not changing over the range $\lambda_c \pm 25$Å. Finally, we add random noise to each spectrum in accordance with the SNR of the observed data, e.g., a mock sample of $N_{\rm spec}$ spectra corresponds to $N_{\rm spec}$ different values of SNR as in the observed spectra. We found that SNR varies across the spectrum in the observed data. For each spectrum we calculate the SNR in 5 different regions and choose the median SNR. We use this observed median SNR in simulated spectra to mimic observations. For comparison, we show a simulated absorption spectrum along a random line of sight through our simulation box in the bottom panel of Fig. 2. One can see that the simulated spectrum is qualitatively quite similar to the observed one (the one with removal of all other lines except Ly-α) shown in the middle panel.

Before proceeding with the analysis of the HST-COS data within the framework of our simulated data it is important to compare our model with those in the literature.

3.4 Comparison with other simulations

We consider three predictions of our simulation that can be used for comparing different simulations. These are (i) fraction of baryons in different phases of the $T - \Delta$ diagram, (ii) predicted IGM equation of state at $z < 0.3$ and (iii) the relationship between H I column density ($N_{\rm HI}$) and baryon overdensity Δ. Some of these predictions depend on the adopted value of $\Gamma_{\rm HI}$. For the present purpose we used $\Gamma_{\rm HI}$ consistent with QSO dominated (i.e. $f_{\rm esc} = 0$) KS15 UVB radiation model.

3.4.1 Phase diagram of baryons

The Ly-α forest is produced by relatively low density and low temperature diffuse gas. According to FGPA the mean Ly-α optical depth is,

$$\tau \propto \Gamma_{\rm HI}^{-1} \, (f_d \, \Omega_b \, h^2)^2 \, \Omega_m^{-0.5}. \quad (8)$$

Thus inferred $\Gamma_{\rm HI}$ from Ly-α will be degenerate with fraction of baryons in diffuse phase (f_d). We found in the literature that different groups use different ranges in T and cutoff in

[6] There is an apparent inconsistency in our analysis because the temperature evolution is calculated for a fixed value of the photoionization rate (e.g., that given by KS15), while we vary the same quantity Γ_{12} at the redshift of interest treating it as a free parameter. This, however, does not affect our results as the obtained gas temperatures (at $z < 0.5$) are insensitive to the assumed value of the Γ_{12} (at $z < 2.1$).

[7] http://www.stsci.edu/hst/cos/performance/spectral_resolution/

Δ to demarcate the phase diagram (i.e., Δ vs T diagram) in 4 phases (see Fig. 5) namely diffuse, WHIM, hot halo and condensed phase. To make a fair comparison with other results we calculate the gas fraction in diffuse and WHIM phase as per the definitions used by the authors under consideration (see Table 2). Smith et al. (2011) label baryons at $z = 0$ as diffuse gas if $T < 10^5$ K and $\Delta < 1000$ and as WHIM if 10^7 K $> T > 10^5$ K and $\Delta < 1000$. We apply the same cutoff at $z = 0$ and find the diffuse and WHIM fraction to be ~ 39.11 per cent and 40.52 per cent respectively which is consistent with the ~ 40 per cent, $40-50$ per cent to that of Smith et al. (2011) and Shull et al. (2015). Note that the moderate feedback processes are included in the AMR (Adoptive Mesh Refinement) simulations of Smith et al. (2011) whereas ours is a SPH simulation without any feedback.

Similarly Davé et al. (2010) have incorporated momentum driven galactic outflows and various other wind models in their SPH simulations (with GADGET) which we lack. They treat baryon particles (at $z = 0$) as part of diffuse if $T < 10^5$ K and $\Delta < 120$ and as a part of WHIM if $T > 10^5$ K and $\Delta < 120$ and found the fraction to be $37-43$ per cent, $23-33$ per cent respectively. By applying similar cutoff on T and Δ at $z = 0$ our diffuse and WHIM fraction turns out to be 34.09 per cent and 28.77 per cent respectively which is in agreement with Davé et al. (2010).

Note that both the set of simulations discussed above have similar resolution like the one we consider here. Unlike our simulations the simulations from the literature discussed above incorporate feedback at different levels. The close matching of baryon fraction in the diffuse phase between different models reiterate the earlier findings that the contribution of feedback effects are minor in the derived $\Gamma_{\rm HI}$ (Davé et al. 2010; Kollmeier et al. 2014; Shull et al. 2015).

3.4.2 Equation of state

The uncertainties in the epoch of He II reionization are reflected in the values of T_0 and γ at the initial redshift $z_1 = 2.1$. To account for this, we vary T_0 and γ at $z_1 = 2.1$ by allowing them to take extreme values (for T_0 and γ measurement at high-z refer Schaye et al. 2000; Lidz et al. 2010; Becker et al. 2011; Boera et al. 2014) and obtain the temperatures at redshifts of our interest using CITE. The resulting values of T_0 and γ at lower redshifts as obtained from the $T-\Delta$ distribution are shown in Table 3. One can see that even for a widely different values of the two parameters at $z_1 = 2.1$, the equation of state at $z \sim 0.1-0.4$ are quite similar with $T_0 \sim 4000-6000$ K and $\gamma \sim 1.5-1.6$. This implies that the low-z IGM loses, to a large extent, any memory of the He II reionization. Our results are consistent with previous simulations by Davé et al. (2010) and Smith et al. (2011) who found that the equation of state parameters at $z = 0$ are $T_0 \sim 5000$ K and $\gamma \sim 1.6$.

The equation of state at low redshifts can be derived by equating net cooling time scale with Hubble timescale. Theuns et al. (1998b) derived such relation (at high z) in low density regime by assuming that the heating rate is dominated by photoheating and cooling rate is dominated by recombination cooling and inverse Compton cooling. The relationship between T and T_0 under this approximation turns out to be,

$$T \sim T_0\, \Delta^{\frac{1}{1+\beta}} \tag{9}$$

While deriving above equation, we have assumed that the H I recombination rate scales as $T^{-\beta}$. For $\beta = 0.7$ the slope of equation of state is $\gamma = 1.59$. This value is very much close to the one we obtained by evolving the IGM temperature using CITE thus validating our method (see Table 3). The mean IGM temperature in the above equation at $z = 0$ is ~ 2555 K (see Eq. C21 in Theuns et al. 1998b). From Table 3, one can see our derived temperatures are higher by factor ~ 2 because Eq. 9 neglects the heating due to other sources such as shock heating, adiabatic heating due to structure formation etc.

The distribution of the CITE temperatures for the gas particles is shown in Fig. 6. The left-hand panel shows the distribution at $z = 0.3$ for different initial values of T_0 and γ. We can see that the distributions at low-z are relatively insensitive to the initial equation of state. Some small differences can be seen at lower temperatures, consistent with the equation of state given in Table 3. The right-hand panel of Fig. 6 shows the CITE temperature distribution at different redshifts for model $T15-\gamma1.3$. As expected, the fraction of shock heated particles increases with decreasing redshift which is a direct consequence of structure formation shocks.

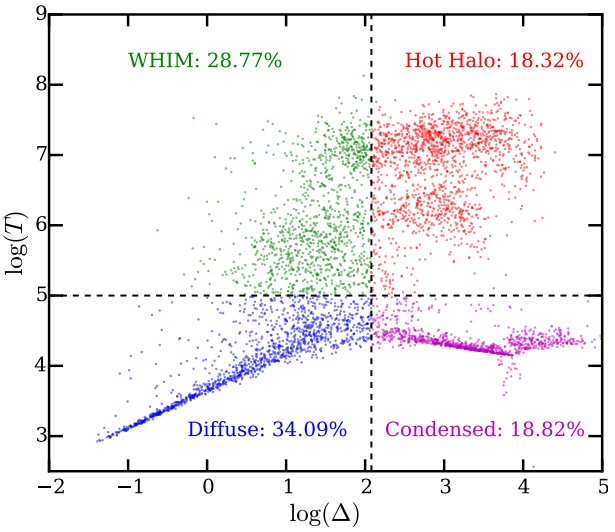

Figure 5. Phase diagram ($T-\Delta$ plane) of randomly selected 20000 GADGET-2 particle post-processed with our module CITE in our simulation at $z = 0$. The black dashed line cutoff at $T = 10^5$ and $\Delta = 120$ demarcates diffuse, WHIM, hot halo and condensed gas phase consistent with Davé et al. (2010) (different authors use different definitions, refer to Table 2 and §3.4 for details). Diffuse gas phase is mainly responsible for the H I absorption seen in the QSO spectrum in the form of Ly-α forest. The percentage of baryons in different phases are given in legend.

3.4.3 Δ vs $N_{\rm HI}$ relation

We further compared our simulations with other simulation using relation between baryon overdensity Δ and H I column density $N_{\rm HI}$. Conventionally this relation is fitted by power-

Table 2. Comparison of predictions of our low-z simulation with those from the literature

Parameters to[1] compare	This Work ($z = 0$)	(Smith et al. 2011) ($z = 0$)	(Davé et al. 2010) ($z = 0$)	Analytical[2] approximation
T_0[a]	3800 - 5100 K	$\sim$ 5000 K	$\sim$ 5000 K	$\sim$ 2555 K
γ[a]	1.46 - 1.62	$\sim$ 1.60	$\sim$ 1.60	$\sim$ 1.58
Diffuse (in per cent)[b]	34.09	-	37 - 43	-
WHIM (in per cent)[b]	28.77	-	23 - 33	-
Diffuse (in per cent)[c]	39.11	$\sim$40	-	-
WHIM (in per cent)[c]	40.52	40 - 50	-	-
Γ_{12}	0.12 ± 0.03	0.122	~ 0.2	0.12 ± 0.03
Δ_0[d]	34.8 ± 5.9	36.9	38.9	20.6 ± 4
α[d]	0.770 ± 0.022	0.650	0.741	0.744 ± 0.015

[a] The range in T_0 and γ corresponds to different initial T_0 (10000 to 25000 K) and γ (1.1 to 1.8) at $z_1 = 2.1$ see Table 3.
[b] WHIM is defined as $T > 10^5$ K and $\Delta < 120$ whereas the diffuse gas phase is defined as $T < 10^5$ K and $\Delta < 120$ in Davé et al. (2010).
[c] WHIM is defined as $10^7\,{\rm K} > T > 10^5$ K and $\Delta < 1000$ whereas the diffuse gas phase is defined as $T < 10^5$ K and $\Delta < 1000$ in Smith et al. (2011) (also refer to Danforth & Shull 2008).
[d] The correlation between baryon overdensity Δ and H I column density is expressed as $\Delta = \Delta_0\, N_{14}^{\alpha}$, where, Δ_0 is the normalization at a fiducial H I column density $N_{\rm HI} = N_{14} \times 10^{14}$ cm^{-2}. This relation is calculated for best fit Γ_{12} in the redshift range $0.2 < z < 0.3$ given in bracket (Fig. 16).
[1] We notice that the Paschos et al. (2009) have presented simulations for low-z IGM. While they check the consistency of the mean transmitted flux for their assumed $\Gamma_{\rm HI}$, no attempt was made to measure $\Gamma_{\rm HI}$. Moreover we could not have detailed comparison with their models as the metric we use for comparison are not available for their models.
[2] $T - \Delta$ relation can be obtained by equating Hubble time with net cooling time (Theuns et al. 1998b). Δ vs $N_{\rm HI}$ is calculated following Schaye (2001) assuming Ly-α clouds are in hydrostatic equilibrium.

Table 3. Details of the thermal history considered in our simulation

	Initial free parameters $z_1 = 2.1$		Final parameters obtained with CITE $z = 0.1$		$z = 0.2$		$z = 0.3$		$z = 0.4$	
Model Name	T_0	γ	T_0	γ	T_0	γ	T_0	γ	T_0	γ
$T10-\gamma1.1$	10000	1.10	4136	1.54	4326	1.53	4589	1.51	4844	1.50
$T10-\gamma1.8$	10000	1.80	4133	1.61	4313	1.61	4568	1.60	4810	1.60
$T20-\gamma1.1$	20000	1.10	4546	1.48	4971	1.46	5383	1.44	5811	1.42
$T20-\gamma1.8$	20000	1.80	4493	1.62	4889	1.62	5279	1.61	5677	1.61
$T15-\gamma1.3$	15000	1.30	4245	1.55	4583	1.54	4902	1.53	5220	1.51

law,

$$\Delta = \Delta_0\, N_{14}^{\alpha} \tag{10}$$

where Δ_0 is the normalization at fiducial H I column density $N_{\rm HI} = N_{14} \times 10^{14}$ cm^{-2}. Assuming hydrostatic equilibrium, Schaye (2001) has derived the above relation analytically for optically thin gas. The normalization and slope of the Δ vs $N_{\rm HI}$ relation is given by,

$$\alpha = \frac{1}{1.5 - 0.26(\gamma - 1)}$$
$$\Delta_0 \sim \left[598\,\Gamma_{12}\,{\rm T}_{0,4}^{0.26}\left(\frac{1.25}{1+z}\right)^{4.5}\left(\frac{0.0221}{\Omega_{\rm b}h^2}\right)^{1.5}\left(\frac{0.16}{f_g}\right)^{0.5}\right]^{\alpha} \tag{11}$$

where γ and $\rm T_{0,4}$ is slope of equation of state and mean IGM temperature in units of 10^4K respectively and f_g is fraction of mass in the gas (excluding stars and molecules). For $\gamma \sim 1.6$, $T_{0,4} \sim 0.45$ and $\Gamma_{12} = 0.12 \pm 0.03$ (for $0.2 < z < 0.3$), the slope and normalization is given as $\alpha \sim 0.744$ and $\Delta_0 = 20.6 \pm 4$. This simple analytic approach is known to produce γ close to what has been seen in the simulations. However, its prediction of the normalization constant need not be accurate as one needs to take care of the baryon fraction in different phases.

To calculate such a relation in simulated spectra we fit the Voigt profile to the absorption lines using our automatic code (see §5.3). To associate the baryon overdensity with absorption line we calculate the optical depth (τ) weighted overdensity $\widetilde{\Delta}$ (Schaye et al. 1999) as follows. Let τ_{ij} be the optical depth contribution of overdensity Δ_i at the wavelength corresponding to the pixel i to the optical depth at pixel j. Then the τ weighted overdensity $\widetilde{\Delta}_j$ at pixel j is given by,

$$\widetilde{\Delta}_j = \frac{\sum_{i=1}^{N} \tau_{ij}\Delta_i}{\sum_{i=1}^{N} \tau_{ij}}, \tag{12}$$

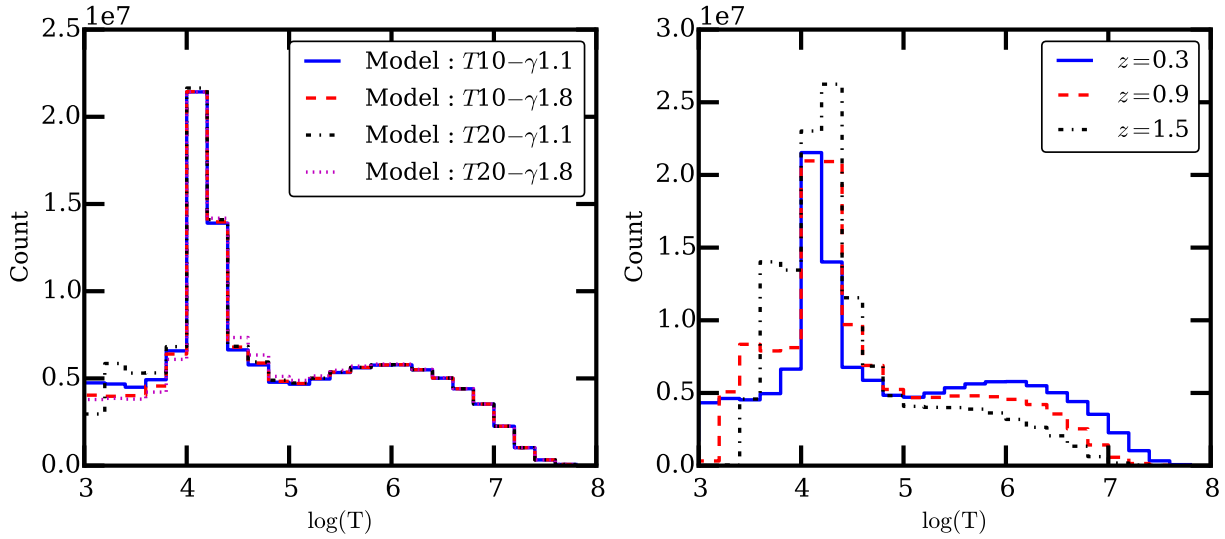

Figure 6. The temperature distribution of the gas particles after using CITE starting from varied initial condition at $z_1 = 2.1$ *Left-hand panel:* the final temperature distribution at $z = 0.3$ for different initial T_0 and γ at $z_1 = 2.1$ (see Table 3). *Right panel:* the temperature distribution at different redshifts $z = 1.5, 0.9, 0.3$. The initial equation of state ($z_1 = 2.1$) for right-hand panel corresponds to model $T15 - \gamma 1.3$ in Table 3.

where N is the total number of pixels in the spectrum. The total optical depth at a pixel j is given by,

$$\tau_j = \sum_{i=1}^{N} \tau_{ij}. \tag{13}$$

Fig. 7 demonstrates our procedure for assigning τ weighted overdensity to an absorption line. 1st,2nd,3rd and 4th panel from top shows flux, overdensity (Δ), temperature (T) and peculiar velocity (v) respectively. The flux in the top panel is calculated from Δ, T and v (all solid blue lines). As expected due to power-law equation of state, Δ and T are correlated (solid blue lines). We calculate the τ weighted temperature by replacing Δ_i in Eq. 11 by T_i. The τ weighted overdensity and the τ weighted temperature (shown by red dashed line in 2nd and 3rd panel from top) are also correlated. We then associate this τ weighted overdensity at the absorption line center to the column density of that line (obtained by Voigt profile fitting). Fig. 8 shows the density plot of τ weighted overdensity Δ and column density $N_{\rm HI}$ for 4000 simulated Ly-α spectra (SNR = 50) in the range $0.2 < z < 0.3$ for $\Gamma_{12} = 0.12$. The magenta errorbar shows the mean τ weighted overdensity (with 1σ error) in each bin of size $\Delta \log N_{\rm HI} = 0.1$. The black dashed line shows the power-law fit with $\Delta_0 = 34.8 \pm 5.9$ and $\alpha = 0.77 \pm 0.022$. The error in Δ_0 corresponds to 1σ range in Γ_{12} (see §5.2). We find that α is less sensitive to Γ_{12}, the error in α accounts for different thermal history (i.e., different values of γ).

The power-law index from our simulation ($\alpha = 0.77 \pm 0.022$) matches well (within 2σ) with Davé et al. (2010) and Tepper-García et al. (2012)($\alpha \sim 0.786$) and theoretically expected values but is slightly higher than Shull et al. (2015) (see Table 2). The normalization parameter Δ_0 in our simulation 34.8 ± 5.9 is in agreement (within 1σ) with Smith et al. (2011); Shull et al. (2015) and Davé et al. (2010) simulation but less than Tepper-García et al. (2012) ($\Delta_0 \sim 48.9$). Note that Tepper-García et al. (2012) used a simulation box with

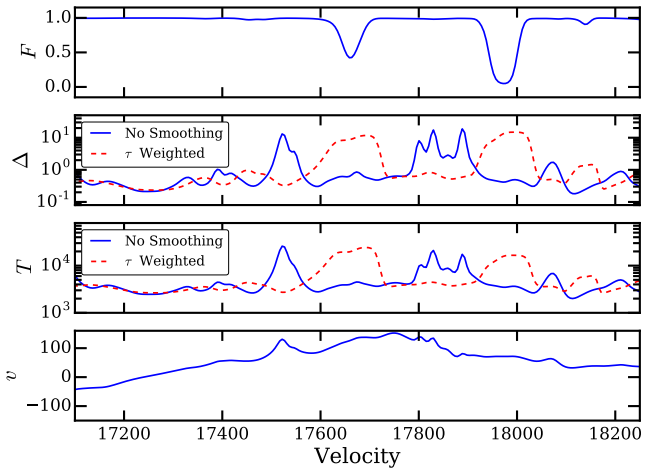

Figure 7. Illustration of assigning optical depth (τ) weighted overdensity and temperature to the absorption lines in simulated spectrum (see §3.4.3). The flux shown in the *top* panel is computed from overdensity (Δ) (blue solid line), temperature (T) (blue solid line) and peculiar velocity (v) (blue solid line) given in 2nd,3rd and 4th panel from top respectively. The τ weighted overdensity (see Eq. 12) and τ weighted temperature are shown by red dashed lines in 2nd and 3rd panel from top respectively. To calculate τ weighted temperature, we replaced Δ_i in Eq. 12 by T_i.

factor 2 lower resolution. Also Δ_0 is sensitive to the value of Γ_{12} used to generate simulated spectra (see Eq. 11).

We also found that the mean flux decrement (DA) calculated from our simulation is within 30 percent to that found from Paschos et al. (2009) and within 20 percent to that from Kollmeier et al. (2014); Viel et al. (2016) when we use their Γ_{12} in our simulations. The higher values of Paschos et al. (2009) can be attributed to the additional heating incorporated in their simulations. Whereas the differences in

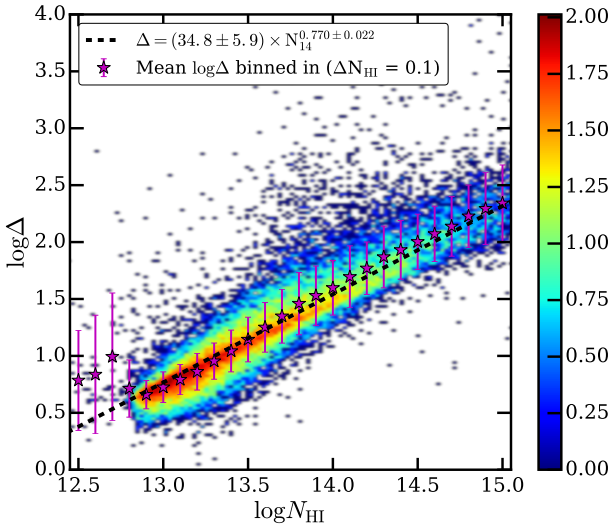

Figure 8. Correlation between τ weighted overdensity Δ (see §3.4.3) and column density $N_{\rm HI}$ for 4000 simulated Ly-α forest spectra (SNR=50) in the range $0.2 < z < 0.3$ for $\Gamma_{12} = 0.12$ (consistent with our final measurements see Fig. 16). The color scheme represents the density of points in logarithmic units. Magenta star points with errorbar are mean τ weighted overdensity binned in $N_{\rm HI}$ with width $\Delta {\rm N_{HI}} = 0.1$. Black dashed line shows our best fit to the mean τ weighted overdensity. The errorbar on best fit values corresponds 1σ variation in Γ_{12} which is 0.03 (see Fig. 16).

DA with Kollmeier et al. (2014); Viel et al. (2016) can be attributed to the differences in fraction of baryons in diffuse phase, mean IGM temperature of the gas in simulation and cosmological parameters used.

We summarize the comparison between our simulation results and others in Table 2. As can be seen, our estimates of T_0 and γ, the fraction of baryons in diffuse gas and in WHIM (accounting for differences in the precise definition), as well as Δ vs $N_{\rm HI}$ relation match quite well with those from other simulations, thus validating our method of evolving the gas temperature using CITE. The advantages of using CITE for the low-z IGM studies are as follows:

- Because CITE is based on post-processing the GADGET-2 output, the method is computationally less expensive.
- CITE allows us to explore large thermal history parameter space without performing the full SPH simulation from high-z.
- We are able to include the ionization and thermal evolution in GADGET-2 as post processing steps.
- It is easy to incorporate the radiative cooling for a wide range of metallicities in CITE.

All these allow us to explore a wide range of parameter space thereby enable us to have a reliable estimation of errors associated with the derived $\Gamma_{\rm HI}$.

3.4.4 Feedback Processes

Our simulations does not include any feedback processes such as galactic winds or AGN feedback. Previously Shull et al. (2015) used the simulations of Smith et al. (2011) which included two types of feedback namely *local* and *distributed* feedback. They found that the phase diagram converges as long as simulation box size $L \geq 50h^{-1}$ cMpc. While the fraction of baryons in WHIM and condensed phase changes considerably with feedback prescription, the fraction of baryons in diffuse phase that is responsible for Ly-α forest remains similar. Because of this they found that both feedback processes affect column density distribution mildly and hence Γ_{12} constraint remains similar (see Fig. 6 in Shull et al. 2015). The feedback method however, can affect the clumpiness of the IGM on small scales whereas large scale correlation between parameters such as Δ and $N_{\rm HI}$ are nearly unaffected. Similarly Davé et al. (2010) and Kollmeier et al. (2014) found that the properties of Ly-α forest are largely insensitive to wind models and feedback prescriptions. Keeping this in mind, now we shall use our simulation to derive $\Gamma_{\rm HI}$ from the HST-COS data.

Despite offering flexibility the obvious shortcoming of CITE is that the diffuse gas is evolved dynamically at effectively zero pressure (because of its low temperature), rather than the pressure it would have if it were at $T \sim 10^4$ K typical of photoionized gas. Thus dynamical impact of diffuse IGM pressure is not modeled self-consistently in CITE. However, the comparisons of CITE with other simulations discussed above suggests that this is not severe shortcoming. The consistency of the phase distribution and the equation of state with other simulations seem almost guaranteed by the nature of CITE. However, the consistency of Δ vs $\rm N_{HI}$ is non-trivial and suggests that the evolving hydrodynamic simulation with low pressure is not distorting the properties of Ly-α forest for the spatial resolution typically achieved in the low-z simulations that are used to reproduce HST-COS data.

4 FLUX STATISTICS

In order to carry out comparison between simulations and observed data at each redshift bin given in Table 1, we consider two statistics of the Ly-α transmitted flux, namely the flux PDF and the flux PS. In the following subsections we describe the method of calculating the flux PDF and PS and appropriate covariance matrix from the simulation.

4.1 Flux PDF

We compute the flux PDF of the observed and simulated spectra for all four redshift bins given in Table 1. We evaluate the distribution using 11 flux bins of width $\Delta F = 0.1$ with the first bin center at $F = 0$ and last one at $F = 1$. The pixels with $F > 1$ (respectively, $F < 0$) are included in the last (respectively, first) bin. Note that the flux bin widths used in this work are larger than those used previously at high-z. This is mainly because the SNR in the present sample is much lower than what is typically achieved in high-z echelle spectra (Jenkins & Ostriker 1991; McDonald et al. 2000; Kim et al. 2007; Desjacques et al. 2007; Bolton et al. 2008; Rollinde et al. 2013). This will influence flux PDF in the bins near continuum and possibly introduce a strong correlation between different bins if bin width is small.

Any meaningful statistical comparison requires errors on the observed flux PDF at each flux bin, along with the

noise covariance between different bins. One standard way of estimating the error covariance matrix from the observed data is to use the jack-knife method. However, we found that the errors obtained using this method are considerably underestimated. This is possibly because the cosmic variance is not properly accounted for in the jack-knife method (Rollinde et al. 2013). Hence, we use the simulated mock samples to compute the covariance matrix as explained below:

As discussed earlier, for each redshift bin (see Table 1) we generate $N = 500$ simulated mock samples for the free parameter Γ_{12} and for each model given in Table 3. We remind the reader that each mock sample consists of number of sightlines equal to observed number of sightlines in the corresponding redshift bin. Let $P_n(F_i)$ denote the value of the flux PDF in the i^{th} bin of n^{th} mock sample, where n takes values from 1 to N. Let the flux PDF in the i^{th} bin averaged over all mock samples be denoted as $\overline{P}_i$. The covariance matrix element $C(i, j)$ between the i^{th} and j^{th} bins is given by,

$$C(i,j) = \frac{1}{N-1} \sum_{n=1}^{N} [P_n(F_i) - \overline{P}_i] \, [P_n(F_j) - \overline{P}_j] \qquad (14)$$

where, i and j can take values from 1 to the number of bins (which in this case is 11). The covariance matrix C is calculated for free parameter Γ_{12} and for each initial $T_0 - \gamma$ (at $z_1 = 2.1$) model given in Table 3.

To visualize the covariance matrix we calculate the correlation matrix defined as

$$Corr(i,j) = \frac{C(i,j)}{\sqrt{C(i,i)\, C(j,j)}}. \qquad (15)$$

The left-hand panel of Fig. 9 shows the correlation matrix for the flux PDF for simulated Ly-α forest at $z = 0.3$ for a model $T15 - \gamma 1.3$ (refer Table 3) and $\Gamma_{12} = 0.1$. It is clear from the figure that the off-diagonal terms of the matrix are not negligible, thus showing that the errors in different bins are correlated. This implies that the full covariance matrix should be used to compute the χ^2 while comparing the simulation with the data. We find that the correlation is strongest for the immediately neighboring bins. Also, the correlation between the neighboring bins increases for higher flux bins since large number of pixels are in the continuum.

In the observed spectra a large number of pixels are found to be in the continuum. Consequently, the errorbar on the flux PDF in the flux bins close to continuum $F \geq 0.9$ are very small. Any χ^2 minimization procedure thus tries to give more weight to the flux PDF bins around $F \geq 0.9$. In addition, these bins near continuum are affected by noise (where, SNR varies from 5 to 15) and continuum fitting uncertainty. This can introduce an additional correlation between bins near the continuum. To avoid such difficulties, during χ^2 minimization we used the flux PDF in the range $0 \leq F \leq 0.8$. However to normalize flux PDF we used all the bins. Note that Rollinde et al. (2013) have used a similar cutoff to calculate the flux PDF at $z \sim 2 - 3$. In our case it is not only the continuum uncertainty but also the relatively poorer SNR of the observed spectra, which affects the flux PDF calculation for bins with $F \geq 0.9$, are important. We have checked and found that ignoring the points near the continuum does not affect our constraints on Γ_{12}, except for a marginal increase in the errorbars on Γ_{12}.

The χ^2, which will be used for quantifying the match between the observed flux PDF and with the simulated one, can be written in the matrix form as,

$$\chi^2_{(T_0,\gamma,\Gamma_{12})} = [P_{(T_0,\gamma,\Gamma_{12})} - P_{obs}] \; C^{-1} \; [P_{(T_0,\gamma,\Gamma_{12})} - P_{obs}]^T, \qquad (16)$$

where P_{obs} denotes observed flux PDF obtained from all the spectra in the relevant redshift bin and $P_{(T_0,\gamma,\Gamma_{12})}$ is the flux PDF obtained from our simulations for a particular model given in Table 3 and a free parameter Γ_{12}. Note that both P_{obs} and $P_{(T_0,\gamma,\Gamma_{12})}$ are row vectors with their i^{th} element being the flux PDF in the i^{th} bin. We re-emphasize that the covariance matrix C is calculated in each redshift bin for each model in Table 3 and Γ_{12}. Note that, because the flux PDF is normalized, the covariance matrix is singular. Hence we use the singular value decomposition method (Press et al. 1992) to compute the χ^2. The $\chi^2_{(T_0,\gamma,\Gamma_{12})}$ can be calculated for each combination of the free parameters $T_0 - \gamma$ at an initial redshift and Γ_{12} at the redshift of our interest. The best-fit parameters are obtained by finding the location of the minimum of the $\chi^2_{(T_0,\gamma,\Gamma_{12})}$. The 1σ confidence level corresponds to the region between $\chi^2_{1\sigma} = \chi^2_{\rm min} \pm \Delta\chi^2_{1\sigma}$, where $\chi^2_{\rm min}$ is the minimum value of the χ^2 and $\Delta\chi^2_{1\sigma} = 1$ (Press et al. 1992).

4.2 Flux PS

We compute the flux PS from observational data and simulations in redshift bins same as those used for estimating the flux PDF. However, there is a crucial difference in how we treat the sightlines while calculating the flux PS from that for the flux PDF. In the case of the flux PDF, we spliced different sightlines from the simulation box to construct a redshift path length as large as the observed redshift range. However, such splicing may introduce spurious effects while computing the two point correlation properties of the flux. Hence for calculating the flux PS we use sightlines of comoving length equal to the simulation box size $50\,h^{-1}$ cMpc. In order to ensure that the simulations and the observations are treated on equal footing, we divide the observed spectra within each z bin into segments which have comoving length equivalent to $50\,h^{-1}$ cMpc. To calculate the flux PS, we first compute the Fourier transform $F(k)$ of the transmitted flux. The corresponding power is given by $P(k) \propto |F(k)|^2$, where the normalisation is calculated from the condition

$$\sigma_F^2 = \int_{-\infty}^{\infty} \frac{dk}{2\pi} \, P(k) \qquad (17)$$

with σ_F^2 being the variance of the transmitted flux. Once we compute $P(k)$ for each segment (of comoving length $50\,h^{-1}$ cMpc) of the spectra, we take an average over all the segments to get an estimate for the flux PS.

A reliable estimate of the flux PS can only be obtained in a limited range of scales because of the finite length of the spectra and other systematic effects. For the observed spectra, the small scale power is affected by the presence of the narrow metal lines (Arinyo-i-Prats et al. 2015). Following McDonald et al. (2000), we choose to work with scales corresponding to $k < k_c \sim 8\ h$ cMpc^{-1}. Similarly, the large scale power in the observed spectra is affected by the uncertainties in the continuum fitting (Kim et al. 2004). In addition,

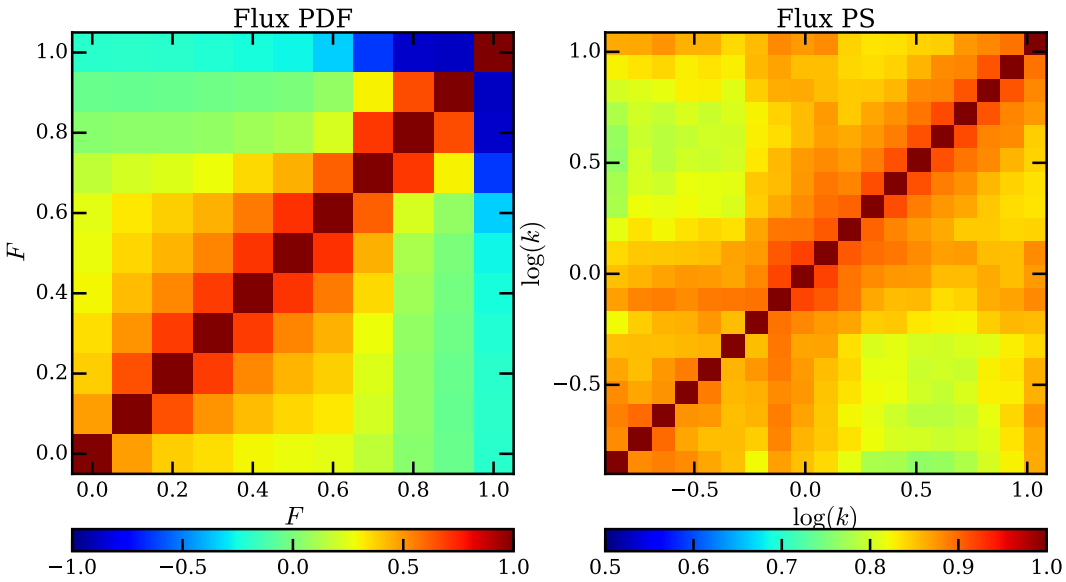

Figure 9. Correlation matrix for the flux PDF (*left-hand panel*) and the flux PS (*right-hand panel*). Both the correlation matrices are calculated using the covariance obtained from the simulated mock samples (see §4.1 and §4.2 for more details). The correlation matrices are shown for simulated Ly-α forest at $z = 0.3$, with $\Gamma_{12} = 0.1$ for $T15 - \gamma 1.3$ model given in Table 3.

while computing the flux PS from our simulations, the finite periodic box size of 50 h^{-1} cMpc implies that scales with $k < k_t \sim 0.2h\,{\rm cMpc}^{-1}$ may not be sampled properly. Hence, to make any meaningful comparison between the observations and simulations we restrict the flux PS measurements to scales $0.209 \leq k/(h\ {\rm cMpc}^{-1}) \leq 8$.

Care must be exercised while binning the $P(k)$ over different k-ranges. We find that for $k \gtrsim 1h\,{\rm cMpc}^{-1}$, the k modes are sampled densely enough to divide the $P(k)$ into bins. In that case we use logarithmic bins of size $\log_{10}(1.24)$ similar to Kim et al. (2004). On the other hand, for $k \lesssim 1h\,{\rm cMpc}^{-1}$, the k modes are sparsely sampled and hence we do not bin the data as done in Arinyo-i-Prats et al. (2015). We ensure that the same procedure is followed while dealing with the observed and simulated spectra.

The procedure for computing the errorbars on the observed flux PS, i.e., estimating the error covariance matrix C, is same as the one discussed for the flux PDF. The matrix C is estimated from the suite of mock spectra. We also attempted to estimate it from the observed spectra using the jack-knife method. However, since the number of observed spectra is relatively small, the off-diagonal terms in the covarinace matrix are found to be noisy. The right-hand panel of Fig. 9 shows the flux PS correlation matrix. The flux PS correlation matrix is dominated by diagonal terms consistent with McDonald et al. (2000) and Zhan et al. (2005). Since the neighboring k-modes are likely to be correlated, the neighboring bins show strong correlation. As one moves away from the diagonal terms the correlations between the different mode decrease. The smaller scales show slightly stronger correlations because the underlying density field is more non-linear and non-gaussian at these scales (Zhan et al. 2005).

We follow the same procedure as discussed in the previous section for calculating χ^2 between model and observed flux PS.

4.3 Tests with the mock spectra

Before using the observed and simulated spectra, to constrain the photoionization rate Γ_{12} at $z < 0.45$, we carry out a few tests on the simulated quantities. First, we check the sensitivity of the flux PDF and flux PS on the parameters $T_0 - \gamma$ (at initial redshift $z_1 = 2.1$) and Γ_{12}. Fig. 10 shows the dependence of the flux PDF (left-hand panel) and flux PS (right-hand panel) at $z = 0.3$ on these three parameters. Note that the values of T_0 and γ at the redshift of interest are obtained by varying these two parameters at the initial redshift $z_1 = 2.1$. The solid and dashed lines, for a given combination of T_0 and γ, in the Fig. 10 correspond to $\Gamma_{12} = 0.08$ and 0.12 respectively at $z \sim 0.3$.

Even though we varied T_0 at $z_1 = 2.1$ by factor of 2, the value of T_0 obtained at $z \sim 0.3$ using CITE differ by only ~ 9 per cent. Similarly, for given T_0 at $z_1 = 2.1$ even when we change initial γ between 1.1 and 1.8 values of T_0 and γ obtained at $z \sim 0.3$ are nearly identical. Thus the flux PDF and PS are fairly insensitive to our choice of $T_0 - \gamma$ at $z_1 = 2.1$. In other words the flux PDF is insensitive to the He II reionization history (also see §3.4.2). It is also clear from Fig. 10 that both the above statistics are sensitive to assumed value Γ_{12}. Therefore they can be used to constrain Γ_{12}.

We next study how well the two statistics can be used for constraining the Γ_{12}. For a particular model given in Table 3 and a fixed value of Γ_{12} (at $z = 0.3$), we construct a mock sample from the simulations, i.e., a set of sightlines which have properties similar to the observed ones. This mock sample can be treated as the "input" data for which the two statistics (flux PDF and PS) can be calculated. We then draw sightlines from other simulation box (parameters T_0 and γ are different from that of the input data) to construct a large number ($N = 500$) of mock samples and compute the two statistics along with the error covariance matrix. The input data and mock samples are drawn from

two different simulation boxes with identical cosmological parameters but different initial conditions. The idea is to vary the value of Γ_{12} for these samples and compare with the input data. The minimization of the χ^2 should enable us to obtain the best-fit value of Γ_{12} along with the errorbars, which can be compared with the input value of Γ_{12}. The result of the analysis for seven different input Γ_{12} values for $z \sim 0.3$ is shown in Fig. 11. The red dashed line indicates the case where there is perfect match between the input and the recovered Γ_{12}. The point with errorbars show the recovered Γ_{12} with the 1σ confidence interval for each input model. We can see that our analysis recovers the input value of the photoionization rate quite accurately. The typical statistical uncertainty in recovering Γ_{12} is ~ 0.015.

Finally, we test the effect of using the HST-COS LSF instead of the traditionally used Gaussian profile function. Fig. 12 shows the flux PDF (*left-hand panel*) and the flux PS (*right-hand panel*) obtained using the two LSFs. The Gaussian LSF used for making this plot has an FWHM = 17 km s^{-1} as shown by solid blue curve. The HST-COS LSF is asymmetric and has extended wings that do not go to zero as rapidly as Gaussian LSF. Hence, the number of pixels near zero are less in HST-COS LSF as compared to Gaussian LSF (*left-hand panel*). The LSF also affects the variance of flux field (σ_F^2) and hence the normalization of flux PS (*right-hand panel*). We found that one would overpredict the Γ_{12} by ~ 20 per cent if the Gaussian LSF is used in the simulated spectra instead of HST-COS LSF using flux PS.

5 RESULTS AND DISCUSSION

5.1 Constraints on Γ_{12}

We obtain constraints on Γ_{12} by comparing the flux PDF and PS from the simulated Ly-α forest with those from the HST-COS data using the χ^2-minimization technique discussed in §4. Fig. 13 shows the results of our analysis for the four redshift bins identified in Fig. 1 and given in Table 1 i.e., for $z = 0.1125, 0.2, 0.3$ and 0.4. T_0 and γ at these redshifts are obtained for different model (see Table 3) by using CITE. For a particular model there is one free parameter Γ_{12} at each z.

The left-hand panels in the Fig. 13 (all results are shown for model $T20-\gamma1.8$) show the comparison of observed flux PDF (red dashed curve) with that of the best fit model (blue dotted curve). The blue shaded regions indicate the 1σ dispersion (i.e., corresponding to diagonal term of the covariance matrix in Eq. 14) in model flux PDF at each value of F calculated from the mock sample. Although we plot the flux PDF in the range 0 to 1, we use only the flux bins $0 \leq F \leq 0.8$ for the χ^2 analysis (as indicated by black dashed vertical line with arrow). We find that the match between the simulated spectra and the observed ones are quite good for all the four redshifts (typical χ^2 per degree of freedom i.e., $\chi^2_{\rm dof} \sim 1$). The only bin where the two do not agree is the bin with $F = 0$ where the observed spectra systematically predict less number of pixels. This mismatch could be due to uncertainty in background subtraction in HST-COS data.

The middle panels show the comparison of observed flux PS (red dashed curve) with best fit model (blue dotted curve). The blue shaded regions indicate the 1σ range

Table 4. Joint (Flux PDF + Flux PS) 1σ constraint on Γ_{12} for different thermal history (see Table 3) for redshift bin I (refer Table 1)

	$z = 0.1$		Joint constraint	
Model	T_0	γ	Γ_{12}[a]	$\chi^2_{\rm dof}$
$T10-\gamma1.1$	4136	1.54	0.067 ± 0.008	0.83
$T10-\gamma1.8$	4133	1.61	0.068 ± 0.007	0.83
$T20-\gamma1.1$	4546	1.48	0.065 ± 0.006	0.81
$T20-\gamma1.8$	4493	1.62	0.066 ± 0.007	0.83
$T15-\gamma1.3$	4245	1.55	0.067 ± 0.008	0.82

[a] The quoted errors are purely statistical.

on the model flux PS. It is interesting to see that the match again is quite good, and we can match both the flux PDF and PS for the same value of Γ_{12}.

The right-hand panels show the variation of the reduced χ^2 with Γ_{12} for the flux PDF (blue dotted curve), the flux PS (red dashed curve) and the combined (i.e., flux PDF and PS) statistics (black solid curve). The best fit Γ_{12} used in the left-hand and middle panels corresponds to the one which gives minimum χ^2 for the combined case. We see that all the three curves have the expected parabolic shape and the reduced χ^2 (i.e., $\chi^2_{\rm dof}$) at the minima have values ~ 1. The minimum of the χ^2 for both the flux PDF and PS occur at similar values of Γ_{12} and agree well within 1σ. We also note that the width of the curve is smaller for the flux PDF alone case than for the flux PS alone case which implies that the flux PDF is better at constraining $\Gamma_{\rm HI}$ than the flux PS. However, flux PDF is sensitive to continuum fitting uncertainty in the HST-COS data, whereas flux PS is less sensitive to it as we will discuss later.

The errors on Γ_{12} obtained using the above method would be an underestimation since it ignores various other effects. We account for possible statistical and systematics uncertainties in Γ_{12} in Table 8. The first of these is the uncertainty in the thermal history, i.e., the two initial parameters T_0 and γ. Ideally one should vary the three parameters simultaneously, obtain the joint likelihood and marginalize over all other parameters except Γ_{12}. However, since we need to solve the temperature evolution for each $T_0 - \gamma$ combination, the full analysis can be quite computationally expensive. Hence we take a slightly different approach where we choose the most extreme values of T_0 and γ at $z_1 = 2.1$ compared to observations Schaye et al. (2000); Becker et al. (2011) and Boera et al. (2014) (for compilation see Puchwein et al. 2015). For each combination of T_0 and γ (given in Table 3), we evolve the thermal history to lower redshifts, compute the Ly-α forest and obtain Γ_{12}. The constraints for different thermal histories for the four redshift bins are summarized in Tables 4, 5, 6 and 7. It is clear from the tables that the constraints on Γ_{12} are relatively insensitive to the values of T_0 and γ at $z_1 = 2.1$. This is what we have seen in Fig. 10. In all cases the differences are small and within statistical uncertainty so for quoting best fit Γ_{12}, we used model $T20-\gamma1.8$ which has minimum χ^2 in three out of four redshift bins.

The constraints on Γ_{12} can also depend on the cosmological parameters, e.g., any change in σ_8 can affect the overall normalization of flux PS since Ly-α flux field and

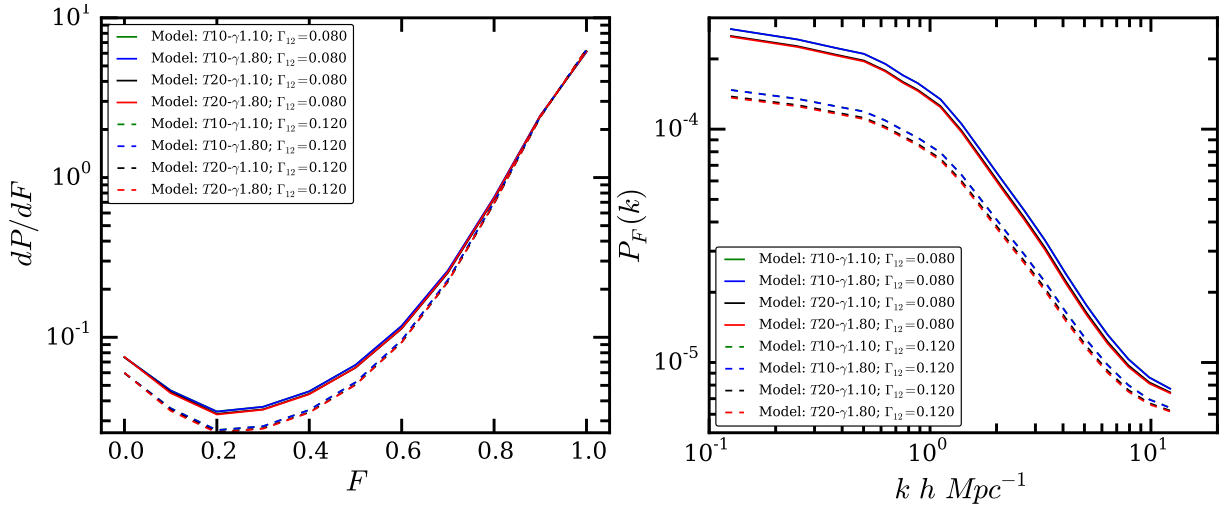

Figure 10. *Left* and *right-hand panels* show respectively the variation of the flux PDF and PS (at $z = 0.3$) for different models given in Table 3 and $\Gamma_{12} = 0.08$ and 0.12 at $z = 0.3$. The values of Γ_{12} and model corresponding to different lines are indicated in the legend. It is clear from the figure that flux PDF and PS are more sensitive to Γ_{12} (at $z = 0.3$) than initial values of T_0 and γ (at $z_1 = 2.1$) because the final equation of states at $z = 0.3$ are very similar (see Table 3).

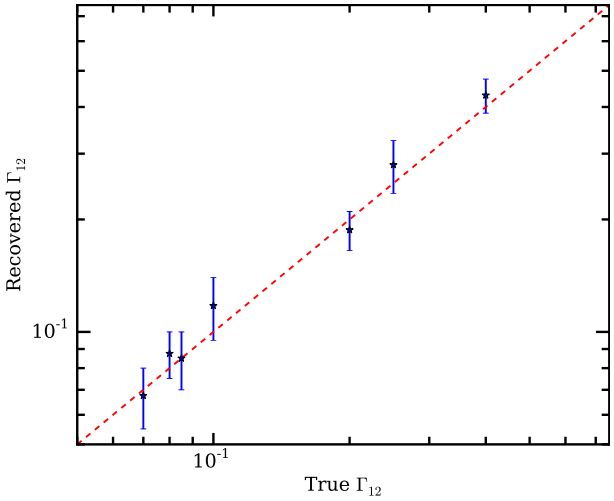

Figure 11. Recovery of the Γ_{12} at $z = 0.3$ using the flux PDF and PS and χ^2 statistics. The x-axis represents the true Γ_{12}, i.e., the one used in the input model. The points with errorbars show the recovered Γ_{12} with the 1σ confidence interval for each input model. The red dashed line indicates the case where there is perfect match between the input and the recovered Γ_{12}. The input and mock data are drawn from two different simulations with same cosmological parameters but different initial condition. The typical uncertainty in recovered Γ_{12} is ± 0.015.

the matter density field are anti-correlated. In order to calculate uncertainty in Γ_{12}, we used Eq. 8 to propagate the error due to uncertainty in cosmological parameters. The uncertainty in cosmological parameters in this work is consistent with Planck Collaboration et al. (2015). We found that the change in Γ_{12} is ≤ 4 per cent due to uncertainty in σ_8 (in the range 0.820 to 0.848). Similarly, uncertainties in $\Omega_{\rm b}h^2$ and Ω_m would also affect the constraints on Γ_{12} (see Eq. 8). The combined uncertainty in Γ_{12} due to uncertainty in $\Omega_{\rm b}h^2$ (in the range 0.02184 to 0.02230) and Ω_m (in the range 0.297 to 0.323) (Planck Collaboration et al. 2015) is

Table 5. Joint (Flux PDF + Flux PS) 1σ constraint on Γ_{12} for different thermal history (see Table 3) for redshift bin II (refer Table 1)

	$z = 0.2$		Joint constraint	
Model	T_0	γ	Γ_{12}[a]	$\chi^2_{\rm dof}$
$T10-\gamma1.1$	4326	1.53	0.105 ± 0.015	1.22
$T10-\gamma1.8$	4313	1.61	0.105 ± 0.015	1.22
$T20-\gamma1.1$	4971	1.46	0.100 ± 0.014	1.13
$T20-\gamma1.8$	4889	1.62	0.100 ± 0.013	1.11
$T15-\gamma1.3$	4583	1.54	0.100 ± 0.015	1.18

[a] The quoted errors are purely statistical.

Table 6. Joint (Flux PDF + Flux PS) 1σ constraint on Γ_{12} for different thermal history (see Table 3) for redshift bin III (refer Table 1)

	$z = 0.3$		Joint constraint	
Model	T_0	γ	Γ_{12}[a]	$\chi^2_{\rm dof}$
$T10-\gamma1.1$	4589	1.51	0.150 ± 0.021	1.05
$T10-\gamma1.8$	4568	1.60	0.150 ± 0.020	1.04
$T20-\gamma1.1$	5383	1.44	0.145 ± 0.023	0.99
$T20-\gamma1.8$	5279	1.61	0.145 ± 0.022	0.99
$T15-\gamma1.3$	4903	1.53	0.145 ± 0.023	1.02

[a] The quoted errors are purely statistical.

~ 4 per cent. Thus we found that the uncertainties in parameters $\Omega_{\rm b}\,h^2$, Ω_m and σ_8 leads to ≤ 10 per cent change in Γ_{12} measurements. Note that we do not account for the correlation between these parameters. We also found that the derived value of Γ_{12} do not change with change in n_s from 0.96 to 1.0.[8]

[8] We performed a GADGET-2 simulation with $n_s = 1.0$ and followed the method described in this paper to constraint Γ_{12}.

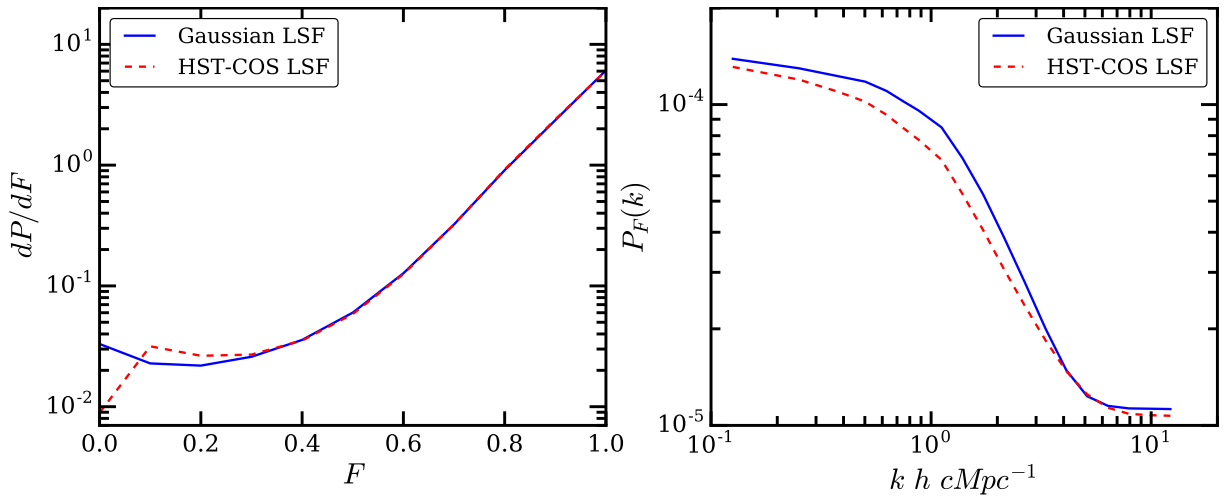

Figure 12. *Left-hand* and *right-hand panels* show the effect of LSF on flux PDF and PS respectively. In both panels results obtained with Gaussian LSF (FWHM ~ 17 km s^{-1}) are shown using solid blue curves and ones that are obtained using HST-COS LSF are shown by red dashed curves. In left-hand panel number of saturated pixels (i.e. $F \sim 0$) are smaller when we use the HST-COS LSF. Right-hand panel shows that the LSF affects the overall normalization (σ_F^2) of the flux PS below $k \sim 6\,h$ cMpc^{-1}.

Table 7. Joint (Flux PDF + Flux PS) 1σ constraint on Γ_{12} for different thermal history (see Table 3) for redshift bin IV (refer Table 1). The Γ_{12} constraints are obtained from Ly-β contamination analysis (see §5.1)

	$z = 0.4$		Joint constraint	
Model	T_0	γ	Γ_{12}[a]	$\chi^2_{\rm dof}$
$T10 - \gamma1.1$	4844	1.5	0.215 ± 0.025	1.09
$T10 - \gamma1.8$	4810	1.6	0.215 ± 0.025	1.08
$T20 - \gamma1.1$	5811	1.42	0.205 ± 0.027	1.01
$T20 - \gamma1.8$	5677	1.61	0.210 ± 0.030	0.96
$T15 - \gamma1.3$	5220	1.51	0.210 ± 0.030	1.06

[a] The quoted errors are purely statistical.

One further source of error could come from the cosmic variance. We use a box having a rather moderate size $50h^{-1}$ cMpc, which could in principle be smaller than the largest voids at $z \sim 0$ (see Fig. 2 in Mao et al. 2016). It is thus possible that our measurements of Γ_{12} may not be globally representative. To account for the effect, we simulate another box of identical size with identical parameters, however choosing a different set of initial conditions on the density and velocity fields. We perform the same statistical analysis on the second box and find that the constraints on Γ_{12} differ by ≤ 3 per cent. This is consistent with the finding of Smith et al. (2011) that simulations do converge for box sizes ≥ 50 cMpc for the number of particles considered in our simulations.

One possible source of uncertainty in $\Gamma_{\rm HI}$ could come from the metallicity of the IGM. At low-z, the IGM is enriched with metals (typical metallicity $\sim 0.1Z_\odot$ see Kulkarni et al. 2005; Shull et al. 2012). In presence of metals the cooling rates are enhanced which in turn can affect the $T - \Delta$ relation. To study the effect of metals on $T - \Delta$ relation, we included the cooling due to metals in CITE using cooling tables given by Wiersma et al. (2009)[9]. We enhance the cooling rates (due to metals) while calculating ionization fractions of species and hence temperature evolution. We do not account for the change in density due to metal cooling in CITE. We assume constant metallicity of $0.1Z_\odot$ from redshift $z_1 = 2.1$ to $z = 0.0$. We found that due to metals the mean IGM temperature T_0 decreases by ~ 10 per cent whereas γ remains same. The fraction of baryons in the diffuse phase increase by ~ 2.5 per cent. Since Γ_{12} constraints are weakly dependent on T_0 and the fractional change in diffuse phase of baryons is small, the IGM metallicity has little effect on Γ_{12}.

The final source of errors on the measured Γ_{12} is the uncertainty in the continuum fitted to the observed spectra. As discussed earlier, each observed spectrum is fitted with the continuum by Danforth et al. (2016). However, because of the limited SNR the continuum fitting procedure is prone to uncertainties. Conventionally, the observed flux is normalized as $F = F_{\rm unnorm}/F_{\rm cont}$, where $F_{\rm unnorm}$ and $F_{\rm cont}$ are the unnormalized and continuum flux, respectively. If $\delta F_{\rm cont}$ is the value of the uncertainty in the continuum, we can calculate the lower and upper bounds on the normalized flux as $F_{\rm lb} = F_{\rm unnorm}/(F_{\rm cont} + \delta F_{\rm cont})$ and $F_{\rm ub} = F_{\rm unnorm}/(F_{\rm cont} - \delta F_{\rm cont})$, respectively. Fig. 15 shows the effect of continuum fitting uncertainties on the observed flux PDF (left-hand panel) and flux PS (right-hand panel). When $\delta F_{\rm cont}$ is taken to be 1σ uncertainty in the continuum, the flux PDF is considerably affected by the continuum uncertainty, whereas the effect on the flux PS is milder and the changes are well within the errorbars. This is the main reason to constrain Γ_{12} from flux PS and flux PDF jointly. In this work, we obtained constraints on Γ_{12} using the three estimates of the transmitted flux F_{lb}, F, and F_{ub} and found that the Γ_{12} range changes systematically by ≤ 10 per cent.

We summarize the total error budget (statistical and systematic) in Table 8. The errors on Γ_{12} are thus calcu-

[9] http://www.strw.leidenuniv.nl/WSS08/

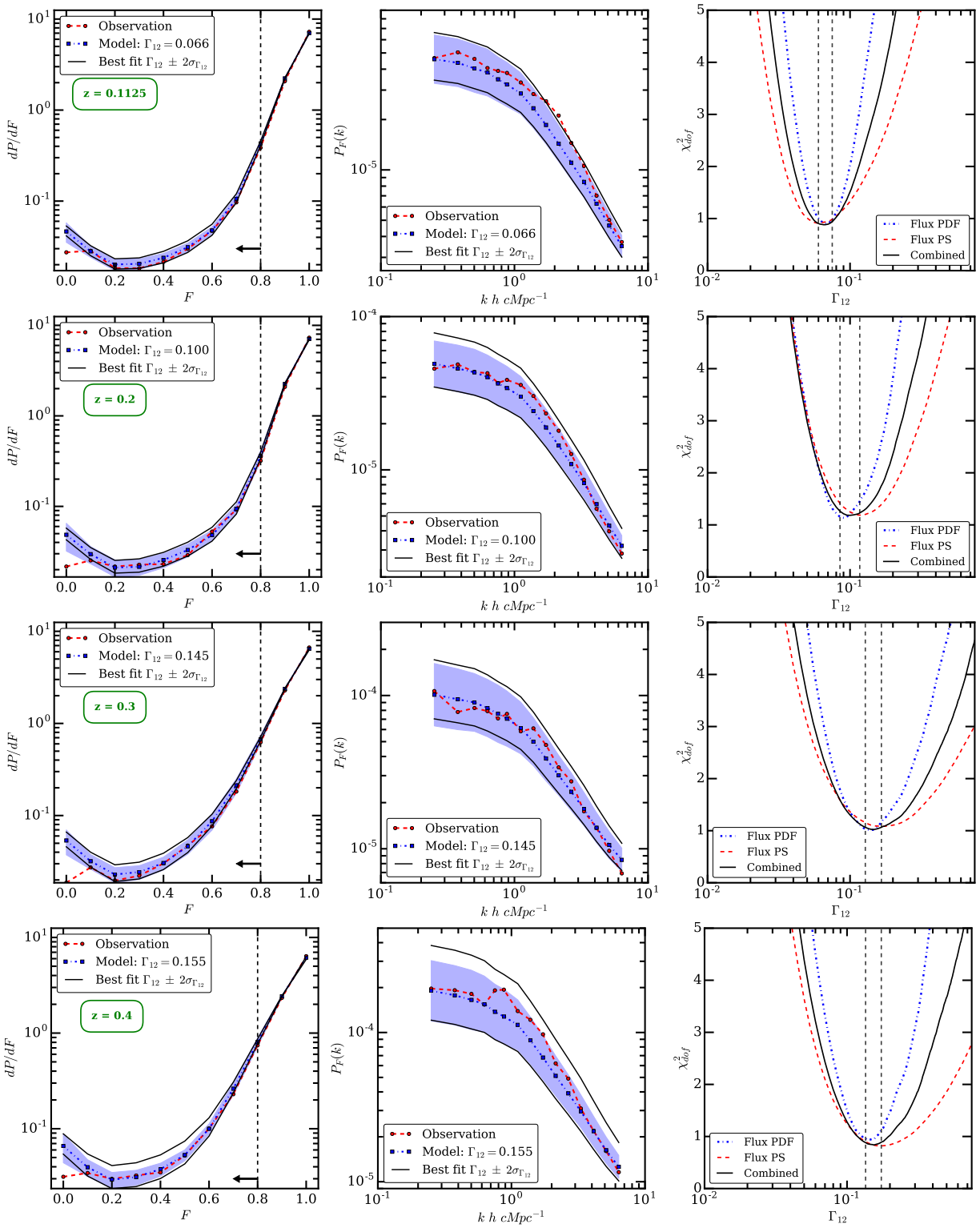

Figure 13. Constraints on Γ_{12} for $z = 0.1125, 0.2, 0.3, 0.4$ from top row to bottom row. The left-hand panels show the flux PDF of observed (red dashed line) and best fit model spectra (blue dotted line). The blue shaded regions show the 1σ range in flux PDF from mock samples covariance matrix (diagonal terms only). The middle panels show the flux PS of observed (red dashed line) and best fit model spectra (blue shaded region). The blue shaded regions show the 1σ range in flux PS from mock samples covariance matrix (diagonal terms only). The right-hand panels show the reduced χ^2 against Γ_{12} for flux PDF (blue dotted curve), flux PS (red dashed curve) and the combined statistics (i.e., flux PDF and PS). The black solid curve is obtained by adding the χ^2 of the flux PDF and PS. Note that the best fit model corresponds to minimum value of joint χ^2_{dof}. The vertical black dashed lines show the 1σ (statistical only) constraint on Γ_{12}. For visual purpose, the model flux PDF and PS obtained by shifting the best fit Γ_{12} by $\pm 2\sigma$ range is shown (black solid line) in the left-hand and middle panel respectively. All the plots are shown for model $T20-\gamma1.8$ (see Table 3). For $z = 0.4$ redshift bin results are shown for the simulated spectra that are *not* contaminated by Ly-β forest (see text and Fig. 14 for details).

lated as follows: (i) We first estimate the error through the χ^2 minimization for the fiducial values of T_0 and γ. (ii) We then account for the uncertainties in T_0 and γ by obtaining constraints for models with extreme values of the two parameters. (iii) We add all statistical uncertainties in quadrature to account for uncertainties in the cosmological parameters, thermal history and cosmic variance. (iv) We finally add total statistical uncertainty with systematic (from the continuum fitting) uncertainty. The Γ_{12} constraints accounting for statistical and systematic uncertainties are given in Table 8.

The redshift bin $z = 0.4$ is likely to be contaminated by Ly-β lines from H I interlopers (Danforth et al. 2016)[10]. The contaminated spectrum will have more absorption hence Γ_{12} would be underpredicted as compared to uncontaminated spectrum. To account for this we contaminated the Ly-α forest (at $z = 0.4$) with Ly-β forest[11] from $z = 0.6$. We have contaminated the region after accounting for observed QSO emission redshift and avoiding proximity region. Fig. 14 shows that Γ_{12} measurement obtained from contaminated spectra are higher as compared to those from uncontaminated spectra (Fig. 13 bottom row). This problem does not arise for other redshift bins because the Ly-β lines are identified based on the Ly-α detected in the HST-COS spectrum and we removed these lines, higher H I Ly-series and metal lines in contaminating line removal process as illustrated in Fig. 2.

5.2 Evolution of Γ_{12}

Having obtained the constraints on Γ_{12} at different redshift bins, we can now try to understand its redshift evolution. Left-hand panel in Fig. 16 shows the constraints on Γ_{12} using the combined χ^2 analysis of flux PDF and PS at the four redshift bins. Blue open circle at $z = 0.4$ in the left-hand panel shows that the Γ_{12} measurements after Ly-β contamination is accounted for properly. We find that there is a clear trend of photoionization rate increasing with increasing redshifts. The best fit values follow $\Gamma_{12} = 0.040 \pm 0.001(1+z)^{4.99\pm0.12}$. Our Γ_{12} constraint at $z = 0.2$ is also in agreement with those obtained from modeling the observed metal abundances by Shull et al. (2014). However, Γ_{12} constraint at $z = 0.1$ are smaller by factor $\sim$ 2.7 as compared to Kollmeier et al. (2014).

To compare our results with the UVB models, we calculate the UVB as explained in Khaire & Srianand (2013) and KS15. The UVB estimate depends on the UV emissivity of QSOs and galaxies and the H I column density distribution, $f(N_{\rm HI}, z)$, of the IGM. We use the QSO emissivity from KS15 at 912 Å (their Eq. 6) obtained using the recent QSO luminosity functions. At $z < 3$, this ϵ_{912} is higher upto factor of 2.2 than the one used by previous UVB models such as Faucher-Giguère et al. (2009); Haardt & Madau (2012, hereafter HM12) which they obtained from the compiled luminosity functions of Hopkins et al. (2007). It is because the recent QSO luminosity function compiled by KS15 from Palanque-Delabrouille et al. (2013); Croom et al. (2009); Schulze et al. (2009) have more bright QSOs. The ratio of the ϵ_{912} from KS15 to the one used by HM12 at $z = 0.1, 0.5, 1.0, 1.5, 2.0, 2.5, 3.0$ is $1.16, 1.61, 2.03, 2.11, 1.86, 1.54, 1.28$ respectively (see Fig. 2 of KS15). The QSO emissivity at $\lambda < 912$ Å depends on the assumed spectral energy distribution (SED) of QSOs. The SED can be approximated by a power-law, $L_\nu \propto \nu^\alpha$, for $\lambda < 912$ Å. We refer to α as UV spectral index. Here, we use $\alpha = -1.4$ from Stevans et al. (2014) as well as $\alpha = -1.7$ from Lusso et al. (2014). Stevans et al. (2014) obtained it by stacking the FUV spectra of 159 QSOs at $0.001 < z < 1.476$ observed with HST-COS which probes rest frame wavelengths down to 475 Å. Whereas, Lusso et al. (2014) obtain it by stacking spectra of a sample of 53 QSOs at $z \sim 2.4$ observed using Wide Field Camera 3 on HST which probes rest wavelength down to 600Å. To model the UVB, we take the galaxy emissivity using a fiducial self-consistent combination of star formation rate density (SFRD) and dust attenuation from Khaire & Srianand (2015b) (as summarized in §3 of Khaire et al. 2016) with $f_{\rm esc}$ being a free parameter. In general, the UVB at $z < 0.5$ has significant contribution coming from high-z sources upto $z \sim 2$ due to steep rise in QSO emissivity as well as SFRD with z. Therefore, we need to constrain the $f_{\rm esc}$ at $z < 2$. For simplicity, we assume a constant $f_{\rm esc}(z)$ over this redshift range.

The $f(N_{\rm HI}, z)$ for $\log N_{\rm HI} > 16$ affects the UVB significantly. It is not well constrained at $z < 2$ due to the small number statistics and because one needs to use spectra obtained with space based observatories. Here, we use recently updated $f(N_{\rm HI}, z)$ from Inoue et al. (2014) which is different than the one used by HM12. For comparison, we calculate UVB using $f(N_{\rm HI}, z)$ of both Inoue et al. (2014) as well as HM12.

The $\Gamma_{\rm HI}(z)$ obtained using these UVB models calculated for two UV spectral indexes and two $f(N_{\rm HI}, z)$ are shown in the right-hand panel of Fig. 16. Here, we assumed $f_{\rm esc}(z)$=0 for $z < 3$ and at $z > 3$ $f_{\rm esc}(z)$ is taken from Khaire et al. (2016). As shown in Fig. 16, all four UVB models are consistent with our low-z $\Gamma_{\rm HI}$ measurements. As can be seen from the figure, QSOs alone are sufficient to explain the $\Gamma_{\rm HI}$ measurements upto $z = 2.5$ (i.e with $f_{\rm esc}(z) = 0$). At higher-z a rapid evolution in $f_{\rm esc}$ is needed as shown in Khaire et al. (2016). We calculate the reduced χ^2 for these UVB models obtained with $f_{\rm esc} = 0$. The UVB with $f(N_{\rm HI}, z)$ of HM12 gives reduced $\chi^2_{\rm dof} = 0.14$ and 1.26 for $\alpha = -1.4$ and $\alpha = -1.7$, respectively. The UVB with $f(N_{\rm HI}, z)$ of Inoue et al. (2014) gives reduced $\chi^2_{\rm dof} = 3.06$ and 0.22 for $\alpha = -1.4$ and $\alpha = -1.7$, respectively.

For UVB model obtained using $f(N_{\rm HI}, z)$ of Inoue et al. (2014) and $\alpha = -1.7$, we find that $f_{\rm esc}(z < 2) = 0.008$ is a conservative 3σ upper limit (with $\Delta\chi^2 \sim 9$). It is consistent with the 3σ upper limits on average $f_{\rm esc} \leq 0.02$ obtained by stacking samples of galaxies (Siana et al. 2010; Cowie et al. 2009; Bridge et al. 2010; Rutkowski et al. 2016). In these observations, lowest average mass of galaxies is $\sim 10^{9.3}$ $M_\odot$ (Rutkowski et al. 2016). It was believed that the UV escape from the lower mass galaxies could be appreciable at all z (Fujita et al. 2003; Razoumov & Sommer-Larsen 2006;

[10] Note that one can still identify such lines using Ly-γ, Ly-δ transition if the Ly-β line is sufficiently saturated. However here we are concerned about the lines which have strong Ly-α and Ly-β transition but weak Ly-γ, Ly-δ transition.

[11] We have only one free parameter Γ_{12} at $z = 0.4$ denoted by $\Gamma_{12,0.4}$ in this analysis. For a given $\Gamma_{12,0.4}$, we obtained $\Gamma_{12,0.6}$ at $z = 0.6$ by using scaling relation $\Gamma_{12,0.6} = \Gamma_{12,\rm norm}(1+z)^{4.4}$ where $\Gamma_{12,\rm norm} = \Gamma_{12,0.4}/1.4^{4.4}$ as found by Shull et al. (2015).

Table 8. Total error budget for our Γ_{12} measurements at different redshifts

Redshift bin ⇒ Type of simulated spectra ⇒	I Ly-α forest	II Ly-α forest	III Ly-α forest	IV Ly-α + Ly-β forest[1]
Best Fit Γ_{12}	0.066	0.100	0.145	0.210
Statistical Uncertainty[a]	± 0.007	± 0.013	± 0.022	± 0.030
Cosmological parameters (∼ 10 per cent) [b]	± 0.007	± 0.010	± 0.015	± 0.021
Cosmic Variance (∼ 3 per cent) [c]	± 0.002	± 0.003	± 0.004	± 0.006
Total statistical errors[d]	± 0.010	± 0.016	± 0.027	± 0.037
Continuum uncertainty (systematic)[e]	± 0.005	± 0.005	± 0.010	± 0.015
Total error[f]	± 0.015	± 0.021	± 0.037	± 0.052

[a] The best fit value and statistical uncertainty is given for the model $T20-\gamma1.8$ (see Table 3) since χ^2 is minimum as compared to other models in 3 out of 4 redshift bins.
[b] Cosmological parameters: Uncertainty due to ($\Omega_b h^2$, Ω_m, σ_8) is (∼ 2 per cent, ∼ 2 per cent, ∼ 4 per cent) respectively. The correlation between different parameters is not accounted for hence the uncertainty is conservative.
[c] To account for cosmic variance, we simulated two different boxes with identical cosmological parameters but with different initial conditions.
[d] All statistical errors are added in quadrature.
[e] This uncertainty arises due to continuum fitting uncertainty. This error is systematic in nature.
[f] Total error is obtained by adding total statistical error with total systematic error.
[1] Simulated Ly-α forest at $z = 0.35$ to 0.45 is contaminated by Ly-β forest in the same wavelength range. The Ly-β forest is generated from simulation box at $z = 0.6$.

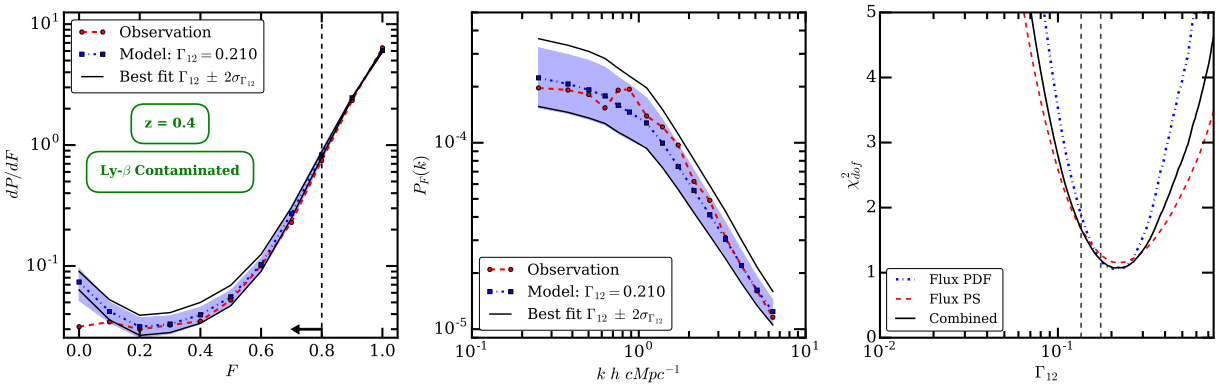

Figure 14. Each panel is same as explained in Fig. 13 except that the Ly-α forest in the redshift range $z = 0.4 \pm 0.05$ is contaminated by Ly-β forest from high redshift ($z = 0.6$). Comparison of the bottom row in Fig. 13 (without Ly-β contamination) with this plot shows that the Γ_{12} constraints are underpredicted (at $z = 0.4$) when Ly-β contamination is not taken into account.

Ferrara & Loeb 2013; Wise et al. 2014) which may solve the problem of higher $f_{\rm esc}$ (∼ 0.15 to 0.2 Mitra et al. 2015; Khaire et al. 2016) at $z > 6$ required for H I reionization. However our derived 3-σ upper limit of $f_{\rm esc}$ is in conjunction with observations of Rutkowski et al. (2016), suggests that galaxies with mass lower than $10^{9.3}$ $M_\odot$ may also have very low $f_{\rm esc}$ providing negligible contributions to the UVB at low-z. It is possible that some additional heating as suggested recently by Viel et al. (2016) may be present and if included that will reduce the derived $\Gamma_{\rm HI}$ further. This will further strengthen our conclusion that QSOs alone are sufficient to provide necessary H I ionizing photons.

5.3 Column density distribution function (CDDF)

The column density distribution (hereafter CDDF) $f(N_{\rm HI}, z)$ is defined as the number of absorbers with column density between $N_{\rm HI}$ to $N_{\rm HI}+dN_{\rm HI}$ and in the redshift range z to $z + dz$.[12] Previously Kollmeier et al. (2014) and Shull et al. (2015) used CDDF to constrain $\Gamma_{\rm HI}$ from Ly-α forest because $f(N_{\rm HI}, z) \propto \Gamma_{12}^{-1}$. To calculate the CDDF, each absorption line is fitted using Voigt profile with column density ($N_{\rm HI}$), doppler b parameter and line center (λ_c) as free parameters. We have developed our own automatic Voigt profile fitting code for Ly-α forest. Following Danforth et al. (2016), we first identify the lines using significance level (SL) cutoff SL > 2 where SL is defined as,

$$\mathrm{SL} = \frac{W(\lambda)}{\sigma(\lambda)} \tag{18}$$

where $W(\lambda)$ and $\sigma(\lambda)$ are equivalent width vector and 'line less error' vector. We then fit all the lines in spectrum si-

[12] Some authors used the absorption path length X instead of redshift z. The two quantities are related by $dX = dz(1+z)^2 \frac{H_0}{H(z)}$ see (Bahcall & Peebles 1969).

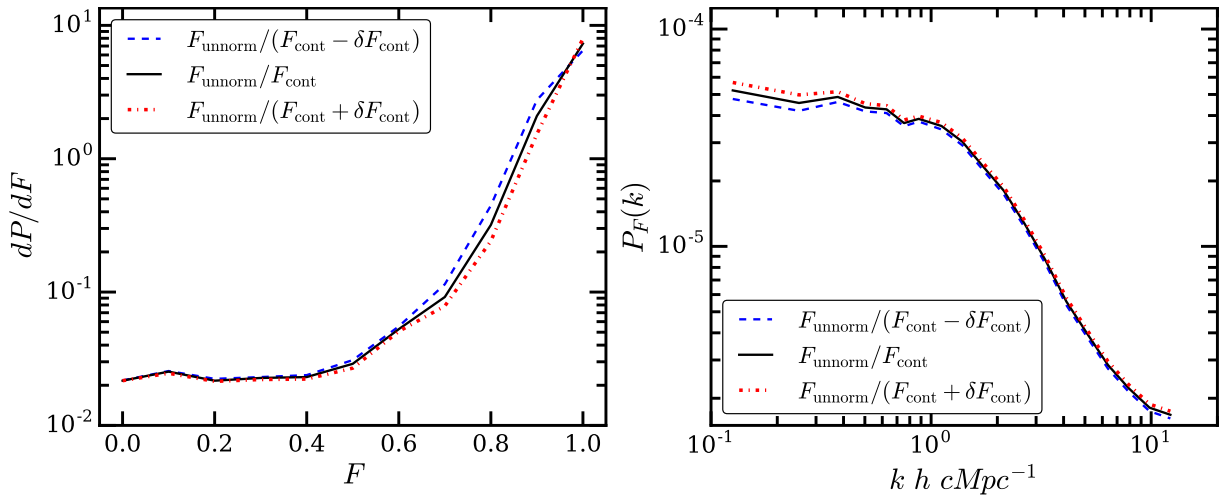

Figure 15. *Left* and *right-hand panels* show variation in flux PDF and PS (for observed spectra at $z = 0.2$) with uncertainty in continuum respectively. $F_{\rm unnorm}$ and $F_{\rm cont}$ are unnormalized and continuum flux respectively. $\delta F_{\rm cont}$ indicates 1σ uncertainty in continuum flux. Due to continuum uncertainty the flux PDF is affected more as compared to flux PS

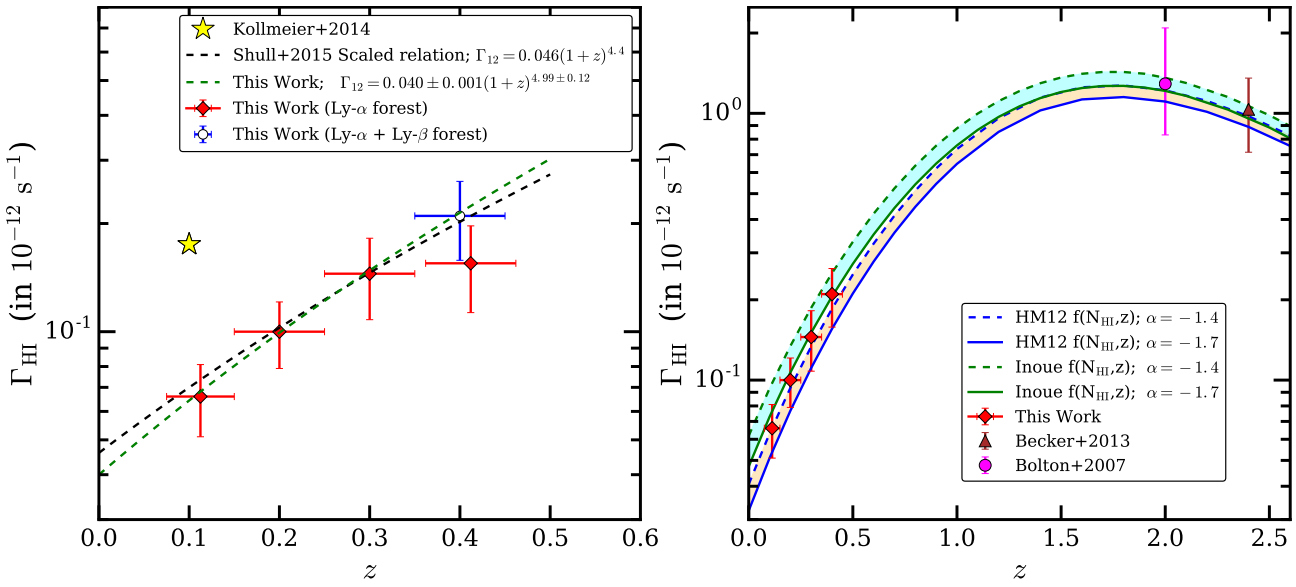

Figure 16. *Left-hand* panel shows the Γ_{12} constraint from joint χ^2 analysis of flux PS and flux PDF. The red diamonds show our Γ_{12} constraints using the simulated Ly-α forest. The last ($z = 0.4$) bin is likely to be affected by Ly-β forest from H I interlopers at high redshift. The blue open circle corresponds to the Γ_{12} constraint using simulated Ly-α forest contaminated by Ly-β forest at $z = 0.6$. A best fit power-law to our measurements is also shown with green dashed line. The scaling relation used by Shull et al. (2015) (black dashed line), where they increased the Γ_{12} evolution of HM12 by a factor 2, is also consistent with our measurements. However our Γ_{12} at $z = 0.1$ is factor ~ 2.7 smaller than Kollmeier et al. (2014) (yellow star). *Right-hand* panel shows the Γ_{12} evolution from $z = 0$ to 2.5 from observations and different UVB models. The cyan and orange shaded regions show evolution of Γ_{12} from KS15 UVB for $f_{\rm esc} = 0$ using Inoue et al. (2014) and HM12 cloud distribution respectively. The shaded region accounts for uncertainty in UV spectral index $\alpha = -1.4$ to -1.7 at $\lambda < 912$ Å. Our results (shown by red diamonds) are consistent with $f_{\rm esc} = 0$ for HM12 and Inoue et al. (2014) cloud distribution allowing for the UV spectral index uncertainties. A constant $f_{\rm esc} = 0$ model (for different cloud distribution and FUV spectral index uncertainty) is sufficient to explain the evolution of Γ_{12} from $z = 0$ to $z = 2.5$ (high-z points are taken from Bolton & Haehnelt (2007) and Becker & Bolton (2013)). All of these predictions use the QSO emissivity of KS15, and no galaxy contribution.

multaneously by allowing parameters to vary in the range $10 \leq \log(N_{\rm HI}) \leq 16.5$, $8 \leq b \leq 150\,{\rm km\,s^{-1}}$ and $\lambda_c \pm 0.1$ Å. As a test to our code we automatically fitted the voigt profiles to the Ly-α lines in the observed HST-COS spectra and found within errorbars most of our fitted parameters agree with Danforth et al. (2016) parameters.[13] We will present the

[13] Danforth et al. (2016) used a semi-automatic technique. For highly saturated lines they fit two or more component and check if fit is improved. The number of such components is small and

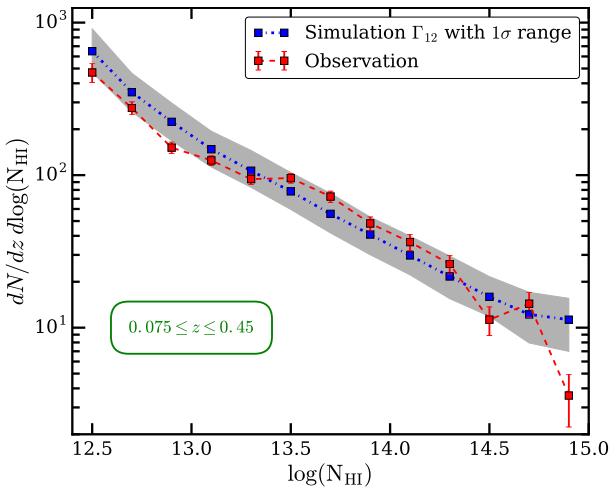

Figure 17. Comparison of CDDF measured from observations (red dashed curve) and our simulations (blue dotted curve) using best fitted $\Gamma_{12}(z)$ in the redshift range $0.075 \leq z \leq 0.45$. The shaded region corresponds to 1σ range in CDDF (obtained by shifting Γ_{12} by $\pm 1\sigma$, see text for more details) that is consistent ($\chi^2_{\rm dof} = 0.85$) with the 1σ constraints on Γ_{12} as a function of z.

detail descriptions and comparison of our code with other codes elsewhere.

Fig. 17 shows the observed CDDF (red dashed line) and simulated CDDF (blue dotted line) in the redshift range $0.075 \leq z \leq 0.45$. We assume that the errorbars on observed CDDF are poisson distributed. The simulated CDDF is calculated from mock suite (mock suite consists of $N \times N_{spec}$ spectra). To calculate the CDDF from simulation (blue dotted line), we used best fit Γ_{12} obtained here (which is evolving with redshift) in the given redshift bin (see Table 8). The shaded region shows the simulated CDDF range obtained by shifting the Γ_{12} by $\pm 1\sigma$ range in Γ_{12} (see Table. 8). From figure it is clear that within errors the observed CDDF and simulated CDDF are consistent with each other. The reduced χ^2 between observed CDDF and simulated CDDF is 0.85 which is also an indication of goodness of fit. For calculating reduced χ^2 we consider only the error in the simulated CDDF and ignore the measurement errors in the observed CDDF. Note that our Γ_{12} measurement at $z = 0.1$ is a factor ~ 2.7 smaller than Kollmeier et al. (2014).

6 SUMMARY

In this work we measure the H I photoionization rate, $\Gamma_{\rm HI}$, at $z \leq 0.45$ using a sample of QSO spectra obtained with Cosmic Origins Spectrograph onboard the Hubble Space Telescope (HST-COS) and hydrodynamical simulations using GADGET-2. We developed a new module "CITE" to evolve the temperature of the IGM from high redshift 2.1 to 0 in the post-processing step of the GADGET-2 simulation taking into account various photo-heating and radiative cooling processes.

We compare our results with other low-z simulations in the literature using three predictions. These are, (i) thermal history parameters: our simulation predicts $T_0 \sim 5000$ K and $\gamma \sim 1.6$ in the redshift range $z = 0.1$ to 0.45. These values are shown to be insensitive to our choice of T_0 and γ at an initial redshift, $z_1 = 2.1$; (ii) distribution of baryons in phase diagram at $z = 0$: We find ~ 34 per cent of baryons are in diffuse phase, ~ 29 per cent in WHIM, ~ 18 per cent in hot halo and ~ 19 per cent in condensed phase and (iii) the correlation between baryon overdensity Δ vs H I column density, $N_{\rm HI}$, in the redshift range $0.2 < z < 0.3$: we find $\Delta = 34.8 \pm 5.9\,(N_{\rm HI}/10^{14})^{0.770\pm0.022}$. We show that all these predictions compare well with those of low-z simulations in the literature that include different feedback processes at varied levels. Feedback processes such and galactic winds or AGN feedback are not incorporated in our simulations. However, as shown by Shull et al. (2015) these processes are not expected to severely influence $\Gamma_{\rm HI}$ constraints. Our method is computationally less expensive and allowed us to quantify various statistical and systematic uncertainties associated with the $\Gamma_{\rm HI}$ measurements.

For fair comparison, we mimic the simulated Ly-α forest as close to observations as possible in terms of SNR, resolution and line spread function. The spectra generated using our method are remarkably similar to the observed spectra. We use two statistics that avoid voigt profile decomposition of the spectra (i.e., flux PDF and PS) and χ^2 minimization using appropriate covariance matrices to compare the observations with the model predictions. Using simulated data we show that these two statistics are good in recovering the $\Gamma_{\rm HI}$. The main results of our work are as follows,

(i) We measured $\Gamma_{\rm HI}$ in four different redshift bins (of $\Delta z = 0.1$) centered at $z = 0.1125, 0.2, 0.3, 0.4$ using joint constraints from the two statistics mentioned above. We estimated the associated errors by varying thermal history parameters, cosmological parameters and continuum fitted to the observed spectrum. Due to limited wavelength range covered in the HST-COS spectrum used in this study, the $\Gamma_{\rm HI}$ measurement for the highest redshift bin (i.e $z = 0.4$) is likely to be affected by the contamination of Ly-β forest absorption from higher-z. We contaminated our simulated Ly-α forest at $z = 0.4$ by Ly-β forest from $z = 0.6$ and corrected for the effect of Ly-β contamination in our $\Gamma_{\rm HI}$ measurement for this z bin. The measured Γ_{12} values at redshift bins $z = 0.1125, 0.2, 0.3, 0.4$ are 0.066 ± 0.015, 0.100 ± 0.021, 0.145 ± 0.037, 0.210 ± 0.052, respectively.

(ii) Our final quoted errors in the $\Gamma_{\rm HI}$ measurements include possible uncertainties coming from the statistical uncertainty[14] ($\sim$ 14 per cent), cosmic variance ($\sim$ 3 per cent), cosmological parameters uncertainty ($\sim$ 10 per cent) and continuum uncertainty (systematic uncertainty $\sim$ 7 per cent). Uncertainty in $\Gamma_{\rm HI}$ due to uncertainty in thermal history parameters, over the range considered here, is small and within statistical uncertainty.

(iii) As expected based on UVB models, even in the small redshift range covered in our study the measured $\Gamma_{\rm HI}$ shows a rapid evolution with z. We fit the redshift evolution of Γ_{12} as $\Gamma_{12} = 0.040 \pm 0.001\ (1+z)^{4.99\pm0.12}$ at $0.075 \leq z \leq 0.45$.

we are using CDDF for consistency check hence we have not incorporated multiple component fit to saturated lines.

[14] The percentage values given in parenthesis are quoted for redshift bin IV i.e., $z = 0.4$ (see Table 8)

(iv) The $\Gamma_{\rm HI}(z)$ obtained here are consistent with the measurement of Shull et al. (2015) however our $\Gamma_{\rm HI}$ measurement at $z = 0.1$ is factor ~ 2.7 smaller than Kollmeier et al. (2014). Note these two earlier measurements used H I column density distribution to constrain $\Gamma_{\rm HI}(z)$. As a consistency check, we show the H I column density distribution predicted by our simulations, for the best fit value of $\Gamma_{12}(z)$ we have obtained using the statistics (flux PDF and PS), matches well with the observed distribution.

(v) The $\Gamma_{\rm HI}$ measurement at any z_1 depends on the emissivities of the ionizing sources at $z \geq z_1$ and Lyman continuum opacity of the IGM. We considered the updated emissivities of QSOs and galaxies (with $f_{\rm esc}$ as a free parameter) and two different H I column density distribution as a function of z obtained by HM12 and Inoue et al. (2014) and obtained $\Gamma_{\rm HI}$ using KS15 UVB code. We find that for, both H I distributions, our derived $\Gamma_{\rm HI}(z)$ is consistent with being contributed only by QSOs. This is true even if we allow for variations in the UV spectral index of QSOs. We also find the maximum 3σ upper limit on $f_{\rm esc}$ at $z < 2$, allowing for uncertainty in FUV spectral index and cloud distribution $f(N_{\rm HI}, z)$ of Inoue et al. (2014), is 0.008. This is consistent with 3σ upper limits on average $f_{\rm esc}$ (i.e ≤ 0.02) obtained by stacking samples of galaxies probing average galaxy mass $M \geq 10^{9.3} M_{\odot}$.

Our measurements suggest that the contribution of low mass galaxies to average $f_{\rm esc}$ will also be small. *Our study confirms that there is no crisis at low redshift in accounting for the observed Lyman continuum photons using standard known luminous astronomical sources.* Thus our $\Gamma_{\rm HI}(z)$ measurement can in turn be used to place a strong constraint on the contributions of decaying dark matter to the low-z UVB.

ACKNOWLEDGMENT

We would like to thank Aseem Paranjape, Sowgat Muzahid and Charles Danforth for useful discussion on statistics and observations. All the computations were performed using the PERSEUS cluster at IUCAA and the HPC cluster at NCRA.

REFERENCES

Adams J. J., Uson J. M., Hill G. J., MacQueen P. J., 2011, ApJ, 728, 107
Arinyo-i-Prats A., Miralda-Escudé J., Viel M., Cen R., 2015, J. Cosmology Astropart. Phys., 12, 017
Bahcall J. N., Peebles P. J. E., 1969, ApJ, 156, L7
Bajtlik S., Duncan R. C., Ostriker J. P., 1988, ApJ, 327, 570
Becker G. D., Bolton J. S., 2013, MNRAS, 436, 1023
Becker R. H., et al., 2001, AJ, 122, 2850
Becker G. D., Bolton J. S., Haehnelt M. G., Sargent W. L. W., 2011, MNRAS, 410, 1096
Benson A., Venkatesan A., Shull J. M., 2013, ApJ, 770, 76
Bergvall N., Zackrisson E., Andersson B.-G., Arnberg D., Masegosa J., Östlin G., 2006, A&A, 448, 513
Bi H., Davidsen A. F., 1997, ApJ, 479, 523
Boera E., Murphy M. T., Becker G. D., Bolton J. S., 2014, MNRAS, 441, 1916
Bolton J. S., Becker G. D., 2009, MNRAS, 398, L26
Bolton J. S., Haehnelt M. G., 2007, MNRAS, 382, 325
Bolton J. S., Haehnelt M. G., Viel M., Springel V., 2005, MNRAS, 357, 1178
Bolton J. S., Haehnelt M. G., Viel M., Carswell R. F., 2006, MNRAS, 366, 1378
Bolton J. S., Viel M., Kim T.-S., Haehnelt M. G., Carswell R. F., 2008, MNRAS, 386, 1131
Bolton J. S., Haehnelt M. G., Warren S. J., Hewett P. C., Mortlock D. J., Venemans B. P., McMahon R. G., Simpson C., 2011, MNRAS, 416, L70
Borthakur S., Heckman T. M., Leitherer C., Overzier R. A., 2014, Science, 346, 216
Boutsia K., et al., 2011, ApJ, 736, 41
Bridge C. R., et al., 2010, ApJ, 720, 465
Calverley A. P., Becker G. D., Haehnelt M. G., Bolton J. S., 2011, MNRAS, 412, 2543
Cen R., Fang T., 2006, ApJ, 650, 573
Cen R., Kimm T., 2015, ApJ, 801, L25
Cen R., Ostriker J. P., 1999, ApJ, 514, 1
Cen R., Ostriker J. P., 2006, ApJ, 650, 560
Cen R., Miralda-Escudé J., Ostriker J. P., Rauch M., 1994, ApJ, 437, L9
Choudhury T. R., Srianand R., Padmanabhan T., 2001, ApJ, 559, 29
Cooke J., Ryan-Weber E. V., Garel T., Díaz C. G., 2014, MNRAS, 441, 837
Cowie L. L., Barger A. J., Trouille L., 2009, ApJ, 692, 1476
Croft R. A. C., Weinberg D. H., Katz N., Hernquist L., 1998, ApJ, 495, 44
Croom S. M., et al., 2009, MNRAS, 399, 1755
Dall'Aglio A., Wisotzki L., Worseck G., 2009, preprint, (arXiv:0906.1484)
Danforth C. W., Shull J. M., 2008, ApJ, 679, 194
Danforth C. W., et al., 2016, ApJ, 817, 111
Davé R., Tripp T. M., 2001, ApJ, 553, 528
Davé R., et al., 2001, ApJ, 552, 473
Davé R., Oppenheimer B. D., Katz N., Kollmeier J. A., Weinberg D. H., 2010, MNRAS, 408, 2051
Deharveng J.-M., Buat V., Le Brun V., Milliard B., Kunth D., Shull J. M., Gry C., 2001, A&A, 375, 805
Desjacques V., Nusser A., Sheth R. K., 2007, MNRAS, 374, 206
Fan X., et al., 2001, AJ, 122, 2833
Fan X., et al., 2006, AJ, 132, 117
Fardal M. A., Giroux M. L., Shull J. M., 1998, AJ, 115, 2206
Faucher-Giguère C.-A., Lidz A., Hernquist L., 2008a, Science, 319, 52
Faucher-Giguère C.-A., Lidz A., Zaldarriaga M., Hernquist L., 2008b, ApJ, 673, 39
Faucher-Giguère C.-A., Lidz A., Hernquist L., Zaldarriaga M., 2008c, ApJ, 682, L9
Faucher-Giguère C.-A., Lidz A., Zaldarriaga M., Hernquist L., 2009, ApJ, 703, 1416
Ferland G. J., Korista K. T., Verner D. A., Ferguson J. W., Kingdon J. B., Verner E. M., 1998, PASP, 110, 761
Fernandez E. R., Shull J. M., 2011, ApJ, 731, 20
Ferrara A., Loeb A., 2013, MNRAS, 431, 2826
Finn C. W., et al., 2016, MNRAS, 460, 590
Fujita A., Martin C. L., Mac Low M.-M., Abel T., 2003, ApJ, 599, 50
Gnedin N. Y., Kravtsov A. V., Chen H.-W., 2008, ApJ, 672, 765
Grazian A., et al., 2016, A&A, 585, A48
Guimarães R., Petitjean P., Rollinde E., de Carvalho R. R., Djorgovski S. G., Srianand R., Aghaee A., Castro S., 2007, MNRAS, 377, 657
Gunn J. E., Peterson B. A., 1965, ApJ, 142, 1633
Haardt F., Madau P., 1996, ApJ, 461, 20
Haardt F., Madau P., 2012, ApJ, 746, 125
Hernquist L., Katz N., Weinberg D. H., Miralda-Escudé J., 1996, ApJ, 457, L51

Hopkins P. F., Richards G. T., Hernquist L., 2007, ApJ, 654, 731
Hui L., Gnedin N. Y., 1997, MNRAS, 292, 27
Inoue A. K., Iwata I., Deharveng J.-M., 2006, MNRAS, 371, L1
Inoue A. K., Shimizu I., Iwata I., Tanaka M., 2014, MNRAS, 442, 1805
Iwata I., et al., 2009, ApJ, 692, 1287
Izotov Y. I., Orlitova I., Schaerer D., Thuan T. X., Verhamme A., Guseva N., Worseck G., 2016, preprint, (arXiv:1601.03068)
Jenkins E. B., Ostriker J. P., 1991, ApJ, 376, 33
Katz N., Weinberg D. H., Hernquist L., 1996, ApJS, 105, 19
Khaire V., Srianand R., 2013, MNRAS, 431, L53
Khaire V., Srianand R., 2015a, MNRAS, 451, L30
Khaire V., Srianand R., 2015b, ApJ, 805, 33
Khaire V., Srianand R., Choudhury T. R., Gaikwad P., 2016, MNRAS, 457, 4051
Kim T.-S., Viel M., Haehnelt M. G., Carswell R. F., Cristiani S., 2004, MNRAS, 347, 355
Kim T.-S., Bolton J. S., Viel M., Haehnelt M. G., Carswell R. F., 2007, MNRAS, 382, 1657
Kim T.-S., Partl A. M., Carswell R. F., Müller V., 2013, A&A, 552, A77
Kirkman D., Tytler D., 2008, MNRAS, 391, 1457
Kollmeier J. A., et al., 2014, ApJ, 789, L32
Kriss G. A., et al., 2001, Science, 293, 1112
Kulkarni V. P., Fall S. M., 1993, ApJ, 413, L63
Kulkarni V. P., Fall S. M., Lauroesch J. T., York D. G., Welty D. E., Khare P., Truran J. W., 2005, ApJ, 618, 68
Kutyrev A. S., Reynolds R. J., 1989, ApJ, 344, L9
Lehner N., Savage B. D., Richter P., Sembach K. R., Tripp T. M., Wakker B. P., 2007, ApJ, 658, 680
Leitet E., Bergvall N., Hayes M., Linné S., Zackrisson E., 2013, A&A, 553, A106
Leitherer C., Hernandez S., Lee J. C., Oey M. S., 2016, ApJ, 823, 64
Lidz A., McQuinn M., Zaldarriaga M., Hernquist L., Dutta S., 2007, ApJ, 670, 39
Lidz A., Faucher-Giguère C.-A., Dall'Aglio A., McQuinn M., Fechner C., Zaldarriaga M., Hernquist L., Dutta S., 2010, ApJ, 718, 199
Lusso E., et al., 2014, ApJ, 784, 176
Madau P., Haardt F., Rees M. J., 1999, ApJ, 514, 648
Madsen G. J., Reynolds R. J., Haffner L. M., Tufte S. L., Maloney P. R., 2001, ApJ, 560, L135
Mao Q., et al., 2016, preprint, (arXiv:1602.02771)
McDonald P., Miralda-Escudé J., Rauch M., Sargent W. L. W., Barlow T. A., Cen R., Ostriker J. P., 2000, ApJ, 543, 1
McDonald P., Miralda-Escudé J., Rauch M., Sargent W. L. W., Barlow T. A., Cen R., 2001, ApJ, 562, 52
Micheva G., Iwata I., Inoue A. K., Matsuda Y., Yamada T., Hayashino T., 2015, preprint, (arXiv:1509.03996)
Miralda-Escude J., Ostriker J. P., 1990, ApJ, 350, 1
Miralda-Escudé J., Cen R., Ostriker J. P., Rauch M., 1996, ApJ, 471, 582
Mitra S., Choudhury T. R., Ferrara A., 2015, MNRAS, 454, L76
Mostardi R. E., Shapley A. E., Steidel C. C., Trainor R. F., Reddy N. A., Siana B., 2015, ApJ, 810, 107
Nestor D. B., Shapley A. E., Kornei K. A., Steidel C. C., Siana B., 2013, ApJ, 765, 47
Oppenheimer B. D., et al., 2016, MNRAS, 460, 2157
Padmanabhan H., Srianand R., Choudhury T. R., 2015, MNRAS, 450, L29
Palanque-Delabrouille N., et al., 2013, A&A, 551, A29
Paschos P., Norman M. L., 2005, ApJ, 631, 59
Paschos P., Jena T., Tytler D., Kirkman D., Norman M. L., 2009, MNRAS, 399, 1934
Planck Collaboration et al., 2015, preprint, (arXiv:1502.01589)
Press W. H., Teukolsky S. A., Vetterling W. T., Flannery B. P., 1992, Numerical Recipes in C (2Nd Ed.): The Art of Scientific Computing. Cambridge University Press, New York, NY, USA
Puchwein E., Bolton J. S., Haehnelt M. G., Madau P., Becker G. D., Haardt F., 2015, MNRAS, 450, 4081
Rahmati A., Schaye J., Crain R. A., Oppenheimer B. D., Schaller M., Theuns T., 2016, MNRAS,
Rauch M., et al., 1997, ApJ, 489, 7
Razoumov A. O., Sommer-Larsen J., 2006, ApJ, 651, L89
Ricotti M., Shull J. M., 2000, ApJ, 542, 548
Robertson B. E., Ellis R. S., Dunlop J. S., McLure R. J., Stark D. P., 2010, Nature, 468, 49
Rollinde E., Srianand R., Theuns T., Petitjean P., Chand H., 2005, MNRAS, 361, 1015
Rollinde E., Theuns T., Schaye J., Pâris I., Petitjean P., 2013, MNRAS, 428, 540
Roy A., Nath B. B., Sharma P., 2015, MNRAS, 451, 1939
Rutkowski M. J., et al., 2016, ApJ, 819, 81
Schaye J., 2001, ApJ, 559, 507
Schaye J., Theuns T., Leonard A., Efstathiou G., 1999, MNRAS, 310, 57
Schaye J., Theuns T., Rauch M., Efstathiou G., Sargent W. L. W., 2000, MNRAS, 318, 817
Schirber M., Miralda-Escudé J., McDonald P., 2004, ApJ, 610, 105
Schulze A., Wisotzki L., Husemann B., 2009, A&A, 507, 781
Scoccimarro R., Hui L., Manera M., Chan K. C., 2012, Phys. Rev. D, 85, 083002
Scott J., Bechtold J., Dobrzycki A., Kulkarni V. P., 2000, ApJS, 130, 67
Shull J. M., 2004, ArXiv Astrophysics e-prints,
Shull J. M., Roberts D., Giroux M. L., Penton S. V., Fardal M. A., 1999, AJ, 118, 1450
Shull J. M., Smith B. D., Danforth C. W., 2012, ApJ, 759, 23
Shull J. M., Danforth C. W., Tilton E. M., 2014, ApJ, 796, 49
Shull J. M., Moloney J., Danforth C. W., Tilton E. M., 2015, ApJ, 811, 3
Siana B., et al., 2010, ApJ, 723, 241
Siana B., et al., 2015, ApJ, 804, 17
Smith B. D., Hallman E. J., Shull J. M., O'Shea B. W., 2011, ApJ, 731, 6
Smith B. M., et al., 2016, preprint, (arXiv:1602.01555)
Songaila A., Bryant W., Cowie L. L., 1989, ApJ, 345, L71
Springel V., 2005, MNRAS, 364, 1105
Srianand R., Khare P., 1996, MNRAS, 280, 767
Stevans M. L., Shull J. M., Danforth C. W., Tilton E. M., 2014, ApJ, 794, 75
Sutherland R. S., Dopita M. A., 1993, ApJS, 88, 253
Tepper-García T., Richter P., Schaye J., Booth C. M., Dalla Vecchia C., Theuns T., 2012, MNRAS, 425, 1640
Theuns T., Leonard A., Efstathiou G., 1998a, MNRAS, 297, L49
Theuns T., Leonard A., Efstathiou G., Pearce F. R., Thomas P. A., 1998b, MNRAS, 301, 478
Theuns T., Bernardi M., Frieman J., Hewett P., Schaye J., Sheth R. K., Subbarao M., 2002, ApJ, 574, L111
Vasei K., et al., 2016, preprint, (arXiv:1603.02309)
Viel M., Haehnelt M. G., Bolton J. S., Kim T.-S., Puchwein E., Nasir F., Wakker B. P., 2016, preprint, (arXiv:1610.02046)
Vogel S. N., Weymann R., Rauch M., Hamilton T., 1995, ApJ, 441, 162
Weinberg D. H., Hernquist L., Katz N., 1997, ApJ, 477, 8
Weinberg D. H., Katz N., Hernquist L., 1998, in Woodward C. E., Shull J. M., Thronson Jr. H. A., eds, Astronomical Society of the Pacific Conference Series Vol. 148, Origins. p. 21 (arXiv:astro-ph/9708213)
Weymann R. J., Vogel S. N., Veilleux S., Epps H. W., 2001, ApJ, 561, 559
Wiersma R. P. C., Schaye J., Smith B. D., 2009, MNRAS, 393, 99

Wise J. H., Demchenko V. G., Halicek M. T., Norman M. L., Turk M. J., Abel T., Smith B. D., 2014, MNRAS, 442, 2560
Worseck G., Prochaska J. X., Hennawi J. F., McQuinn M., 2014, preprint, (arXiv:1405.7405)
Zhan H., Davé R., Eisenstein D., Katz N., 2005, MNRAS, 363, 1145
Zhang Y., Anninos P., Norman M. L., 1995, ApJ, 453, L57
Zheng W., et al., 2004, ApJ, 605, 631

APPENDIX

We tabulate the flux PDF, the PS and mean flux decrement (DA) obtained from the observational data used in this paper, and also the values corresponding to our best-fit model. The errors on flux PDF and flux PS are obtained from the simulated mock samples.

Mean flux decrement: Following the standard definition the mean flux decrement along a sightline is given by,

$$\mathrm{DA} = \langle 1 - \mathrm{e}^{-\tau} \rangle \tag{19}$$

where $\mathrm{e}^{-\tau}$ is normalized flux and angle brackets represent average along the wavelength. The total mean flux decrement for the N sightlines is given by,

$$\mathrm{DA}_{\mathrm{sample}} = \frac{1}{N} \sum_{i=1}^{N} \mathrm{DA}_i \tag{20}$$

where DA_i is mean flux decrement along i^{th} sightline. The variance ($\sigma^2_{\mathrm{sample}}$) of the total mean flux decrement for the N sightlines is given by,

$$\sigma^2_{\mathrm{sample}} = \frac{1}{N} \sum_{i=1}^{N} (\mathrm{DA}_i - \mathrm{DA}_{\mathrm{sample}})^2 \tag{21}$$

Table 11 shows the observed ($\mathrm{DA}_{\mathrm{data}}$) and best fit flux decrement ($\mathrm{DA}_{\mathrm{model}}$) from our simulation for different redshift bins (calculated using Eq. 20). The uncertainty in $\mathrm{DA}_{\mathrm{data}}$ is calculated using Eq. 21 whereas the uncertainty in $\mathrm{DA}_{\mathrm{model}}$ corresponds to 1σ uncertainty in best fit Γ_{12}. The uncertainty in $\mathrm{DA}_{\mathrm{data}}$ due to continuum fitting uncertainty is not accounted for. Note that for χ^2 analysis, we used flux PDF in the range $F \leq 0.85$.

This paper has been typeset from a TEX/LATEX file prepared by the author.

Table 9. The observed and best fit Γ_{12} (see Table 8) flux PDF from our simulation for redshift bins. The errorbars on model flux PDF indicate diagonal terms of the covariance matrix. The covariance matrix can be available on request.

Spectra →	Ly-α forest		Ly-α forest		Ly-α forest		Ly-α + Ly-β forest	
	$z = 0.1125$	$z = 0.1125$	$z = 0.2$	$z = 0.2$	$z = 0.3$	$z = 0.3$	$z = 0.4$	$z = 0.4$
F	$P_{\rm data}$	$P_{\rm model} \pm dP_{\rm model}$	$P_{\rm data}$	$P_{\rm model} \pm dP_{\rm model}$	$P_{\rm data}$	$P_{\rm model} \pm dP_{\rm model}$	$P_{\rm data}$	$P_{\rm model} \pm dP_{\rm model}$
0	0.027	0.046 ± 0.011	0.022	0.049 ± 0.016	0.019	0.054 ± 0.016	0.031	0.074 ± 0.022
0.1	0.028	0.028 ± 0.004	0.025	0.030 ± 0.006	0.027	0.032 ± 0.006	0.034	0.042 ± 0.008
0.2	0.018	0.020 ± 0.003	0.022	0.021 ± 0.005	0.020	0.023 ± 0.004	0.030	0.031 ± 0.006
0.3	0.018	0.020 ± 0.003	0.023	0.022 ± 0.004	0.022	0.024 ± 0.004	0.032	0.033 ± 0.006
0.4	0.021	0.024 ± 0.003	0.023	0.026 ± 0.005	0.030	0.030 ± 0.005	0.035	0.039 ± 0.006
0.5	0.030	0.031 ± 0.003	0.029	0.033 ± 0.005	0.047	0.046 ± 0.008	0.052	0.056 ± 0.007
0.6	0.047	0.048 ± 0.004	0.053	0.048 ± 0.006	0.077	0.087 ± 0.017	0.100	0.103 ± 0.013
0.7	0.097	0.106 ± 0.010	0.092	0.094 ± 0.011	0.182	0.212 ± 0.038	0.229	0.271 ± 0.039
0.8	0.386	0.429 ± 0.037	0.319	0.362 ± 0.050	0.626	0.674 ± 0.073	0.745	0.828 ± 0.086
0.9	2.079	2.229 ± 0.057	2.093	2.250 ± 0.083	2.282	2.379 ± 0.052	2.334	2.458 ± 0.051
1	7.247	7.018 ± 0.094	7.300	7.066 ± 0.134	6.668	6.439 ± 0.112	6.375	6.065 ± 0.116

Table 10. The observed and best fit Γ_{12} (see Table 8) flux PS from our simulation for redshift bins. The errorbars on model flux PS indicate diagonal terms of the covariance matrix. The covariance matrix can be available on request. The wavenumber k is expressed in units of h cMpc^{-1}.

Spectra →	Ly-α forest		Ly-α forest		Ly-α forest		Ly-α + Ly-β forest	
	$z = 0.1125$	$z = 0.1125$	$z = 0.2$	$z = 0.2$	$z = 0.3$	$z = 0.3$	$z = 0.4$	$z = 0.4$
$\log k$	Data $\log P_F$	Model $\log P_F \pm$ dlog P_F	Data $\log P_F$	Model $\log P_F \pm$ dlog P_F	Data $\log P_F$	Model $\log P_F \pm$ dlog P_F	Data $\log P_F$	Model $\log P_F \pm$ dlog P_F
−0.601	−4.332	-4.338 ± 0.145	−4.340	-4.308 ± 0.149	−3.971	-3.995 ± 0.204	−3.706	-3.652 ± 0.162
−0.425	−4.297	-4.360 ± 0.142	−4.312	-4.339 ± 0.153	−4.107	-4.025 ± 0.198	−3.717	-3.685 ± 0.158
−0.300	−4.337	-4.394 ± 0.143	−4.361	-4.364 ± 0.151	−4.082	-4.045 ± 0.189	−3.741	-3.716 ± 0.158
−0.203	−4.391	-4.418 ± 0.140	−4.369	-4.395 ± 0.144	−4.102	-4.082 ± 0.187	−3.813	-3.749 ± 0.155
−0.124	−4.408	-4.459 ± 0.133	−4.433	-4.436 ± 0.145	−4.150	-4.119 ± 0.187	−3.718	-3.799 ± 0.151
−0.057	−4.421	-4.490 ± 0.132	−4.413	-4.466 ± 0.141	−4.120	-4.151 ± 0.180	−3.713	-3.835 ± 0.148
0.047	−4.477	-4.543 ± 0.123	−4.446	-4.521 ± 0.131	−4.234	-4.212 ± 0.169	−3.857	-3.894 ± 0.135
0.142	−4.547	-4.632 ± 0.119	−4.518	-4.616 ± 0.123	−4.214	-4.302 ± 0.157	−3.915	-4.002 ± 0.128
0.236	−4.589	-4.732 ± 0.114	−4.633	-4.724 ± 0.120	−4.323	-4.411 ± 0.146	−4.012	-4.127 ± 0.117
0.331	−4.675	-4.843 ± 0.108	−4.745	-4.842 ± 0.111	−4.469	-4.521 ± 0.130	−4.207	-4.257 ± 0.110
0.425	−4.839	-4.957 ± 0.100	−4.897	-4.963 ± 0.101	−4.560	-4.628 ± 0.123	−4.309	-4.386 ± 0.099
0.520	−4.977	-5.072 ± 0.092	−5.064	-5.087 ± 0.095	−4.756	-4.741 ± 0.109	−4.509	-4.517 ± 0.089
0.615	−5.154	-5.202 ± 0.083	−5.254	-5.224 ± 0.085	−4.864	-4.863 ± 0.098	−4.658	-4.657 ± 0.081
0.709	−5.299	-5.333 ± 0.075	−5.401	-5.364 ± 0.077	−5.013	-4.976 ± 0.089	−4.794	-4.791 ± 0.071
0.804	−5.431	-5.456 ± 0.065	−5.546	-5.496 ± 0.067	−5.161	-5.073 ± 0.077	−4.936	-4.906 ± 0.063

Table 11. The observed ($DA_{\rm data}$) and best fit flux decrement ($DA_{\rm model}$) from our simulation for different redshift bins.

Redshift bin ⇒ Type of simulated spectra ⇒	I Ly-α forest	II Ly-α forest	III Ly-α forest	IV Ly-α + Ly-β forest[a]
Best Fit Γ_{12}	0.066 ± 0.015	0.100 ± 0.021	0.145 ± 0.037	0.210 ± 0.052
$DA_{\rm data}$[b]	0.021 ± 0.002	0.024 ± 0.002	0.025 ± 0.002	0.031 ± 0.003
$DA_{\rm model}$[c]	0.028 ± 0.005	0.030 ± 0.004	0.032 ± 0.006	0.033 ± 0.006

[a] Simulated Ly-α forest at $z = 0.35$ to 0.45 is contaminated by Ly-β forest in the same wavelength range. The Ly-β forest is generated from simulation box at $z = 0.6$.
[b] The uncertainty in $DA_{\rm data}$ is calculated using Eq. 21. However, the uncertainty in $DA_{\rm data}$ due to continuum fitting uncertainty is not accounted for. Note that for χ^2 analysis, we used flux PDF in the range $F \leq 0.85$.
[c] The uncertainty in $DA_{\rm model}$ corresponds to 1σ uncertainty in best fit Γ_{12}.